MICROWAVE SCATTERING FOR DIAGNOSTICS OF LASER-INDUCED PLASMAS AND DENSITIES OF SPECIES IN COMBUSTION MIXTURES

by

Animesh Sharma

A Dissertation

Submitted to the Faculty of Purdue University

In Partial Fulfillment of the Requirements for the degree of

Doctor of Philosophy

School of Aeronautics and Astronautics

West Lafayette, Indiana

August 2020

THE PURDUE UNIVERSITY GRADUATE SCHOOL
STATEMENT OF COMMITTEE APPROVAL

Dr. Alexey Shashurin, Chair
School of Aeronautics and Astronautics

Dr. Mikhail N. Slipchenko
School of Aeronautics and Astronautics

Dr. Sergey O. Macheret
School of Aeronautics and Astronautics

Dr. Allen Garner
School of Nuclear Engineering

Approved by:
Dr. Gregory A. Blaisdell

To

My parents,

Anu and Amit Sharma

&

My brother,

Krishna Sharma

Your encouragement and support

Helps me persevere

ACKNOWLEDGMENTS

First and foremost, I would like to express my deepest gratitude towards my advisor Dr. Alexey Shashurin. I am extremely grateful for all the effort and time he spent honing my skills along with all the opportunities he provided me during my graduate program. The completion of this journey would not have been possible without his unwavering support, untiring patience and invaluable guidance.

I very much appreciate Dr. Mikhail Slipchenko, Dr. Sergey Macheret and Dr. Allen Garner for their time serving as the committee members. Dr. Slipchenko's challenging questions and inputs during our discussions and experiments along with his unparalleled knowledge for lasers and optics has been paramount in realization of this work. Dr. Garner's comments and feedback on my dissertation has been extremely helpful. Furthermore, I sincerely appreciate the opportunity to work with Dr. Vikas Tomar, Dr. Alina Alexeenko, Dr. John Sullivan and Dr. James Garrison during my graduate program.

Many thanks go to my fellow graduate students Xingxing Wang and Yunping Zhang at Electric Propulsion and Plasma Laboratory. Especially, Xingxing Wang for his help when was starting and for the numerous discussions along the way. I also had pleasure working with Arafat Rahman, Erik Braun, Karna Patel and Daniel Lauriola at Maurice J. Zucrow Laboratories. Particularly Rahman and Erik Braun for extending great amount of assistance.

I would like to recognize the assistance of the staff, Delaney Morgan, Xiaomin Qian, Beverly Clenden and Amanda Dalton during my time spent at School of Aeronautics and Astronautics.

I would like to acknowledge the Research Assistantship provided by Dr. Shashurin and Teaching Assistantship provided by School of Aeronautics and Astronautics for financially supporting my graduate program.

TABLE OF CONTENTS

LIST OF TABLES

LIST OF FIGURES

SYMBOLS

γ	Keldysh Parameter
ω	Angular frequency
ω_t	Tunneling frequency
$\mathcal{E}_i$	Ionization potential Energy
I	Laser irradiance
I_0	laser irradiance at the center of beam waist
m	mass of electrons
e	Charge of electron
n_e	Electron number density
n_0	Number density in ground state
n_i	Number density of i^{th} level
n_M	Number density of species *M*
N_e	Total number of electrons
λ	Wavelength
w	Beam radius
w_0	Beam waist radius
z_R	Rayleigh length of laser
ε	Dielectric constant of a material
ε_0	Dielectric permittivity of free space
p	Dipole moment
V	Volume
c	Speed of light in vacuum
ν	Collision frequency
A	Calibration constant
ω	Angular frequency of microwave radiation

U_{out}	Output of RMS system
σ_8	Cross 8 photon ionization process
k	Three body conversion ionization rate
β	Three body recombination rate
ν_a	Electron attachment rate
Q_{ij}	Quenching rates
A_{ij}	Spontaneous emission rates
σ_2	Cross section for 2 photon, 8 photon, ionization process
σ_{ion}	Cross section for ionization process
W_{13}	Rate of two photon absorption from level 1 to level 3
P_{ion}	Ionization rate
τ	Characteristic time scale
Ar	Argon
Kr	Krypton
Xe	Xenon
O_2	Oxygen molecule
N_2	Nitrogen molecule
CO	Carbon Monoxide

ABBREVIATIONS

TI	Tunneling Ionization
MPI	Multiphoton Ionization
REMPI	Resonance enhanced multiphoton ionization
MS	Microwave Scattering
RMS	Rayleigh Microwave scattering
TPA	Two-Photon Absorption
LIF	Laser Induced Fluorescence
TOF	Time of Flight
CARS	Coherent Anti-Stokes Raman Scattering
Fs-laser	Femtosecond laser

ABSTRACT

Laser-induced plasmas since their discovery in the 1960's have found numerous applications in laboratories and industries. Their uses range from soft ionization source in mass spectroscopy, development of compact particle accelerator, and X-ray and deep UV radiation sources to diagnostic techniques such as laser-induced breakdown spectroscopy and laser electronic excitation tagging. In addition, the laser-induced plasma is important for studying of various nonlinear effects at beam propagation, such as laser pulse filamentation.

This work deals with two challenging aspects associated with laser-induced plasmas. First is the study of Multi-Photon Ionization (MPI) as a fundamental first step in high-energy laser-matter interaction critical for understanding of the mechanism of plasma formation. The second is application of laser induced plasma for diagnostics of combustion systems.

Numerous attempts to determine the basic physical constants of MPI process in direct experiments, namely photoionization rates and cross-sections of the MPI, were made; however, no reliable data was available until now, and the spread in the literature values often reached 2–3 orders of magnitude. This work presents the use of microwave scattering in quasi-Rayleigh regime off the electrons in the laser-induced plasma as method to measure the total number of electrons created due to the photoionization process and subsequently determine the cross-sections and rates of MPI. Experiments were done in air, O_2, *Xe, Ar,* N_2, *Kr*, and *CO* at room temperature and atmospheric pressure and femtosecond-laser pulse at 800 nm wavelength was utilized. Rayleigh microwave scattering (RMS) technique was used to obtain temporally resolved measurements of the electron numbers created by the laser. Numbers of electrons in the range 3×10^8–3×10^{12} were produced by the laser pulse energies 100–700 μJ and corresponding electron number densities

down to about 10^{14} cm^{-3} in the center of laser-induced spark were observed. After the laser pulse, plasma decayed on the time scale from 1 to 40 ns depending on the gas type and governed by two competing processes, namely, the creation of new electrons from ionization of the metastable atoms and loss of the electrons due to dissociative recombination and attachment to oxygen.

Diagnostics of combustion at high pressures are challenging due to increased collisional quenching and associated loss of acquired signal. In this work, resonance enhanced multiphoton photon ionization (REMPI) in conjunction with measurement of generated electrons by RMS technique were used to develop diagnostics method for measuring concentration of a component in gaseous mixture at elected pressure. Specifically, the REMPI-RMS diagnostics was developed and tested in the measurements of number density of carbon monoxide (*CO*) in mixtures with nitrogen (N_2) at pressures up to 5 bars. Number of REMPI-induced electrons scaled linearly with *CO* number density up to about $5 \cdot 10^{18}$ cm^{-3} independently of buffer gas pressure up to 5 bar, and this linear scaling region can be readily used for diagnostics purposes. Higher *CO* number densities were associated laser beam energy loss while travelling through the gaseous mixture. Four (4) energy level model of *CO* molecule was developed and direct measurements of the laser pulse energy absorbed in the two-photon process during the passage through the CO/N_2 mixture were conducted in order to analyze the observed trends of number of REMPI-generated electrons with *CO* number density and laser energy.

1. INTRODUCTION

1.1 Lasers

Lasers is an acronym which stands for light amplification by stimulated emission of radiation. They are devices that generate and/or amplify coherent radiation at frequencies in the IR, visible UV region soft electromagnetic spectrum. Their operation is based on the same general principles which were originally developed for microwave frequencies.

The development of the first such source in the optical regime is attributed to Maiman in 1960.[1] He constructed the first laser using a cylinder of synthetic ruby measuring 1 cm in diameter and 2 cm long, with the ends silver-coated to make them reflective and able to serve as a Fabry-Perot resonator. Maiman used photographic flashlamps as the laser's pump source.

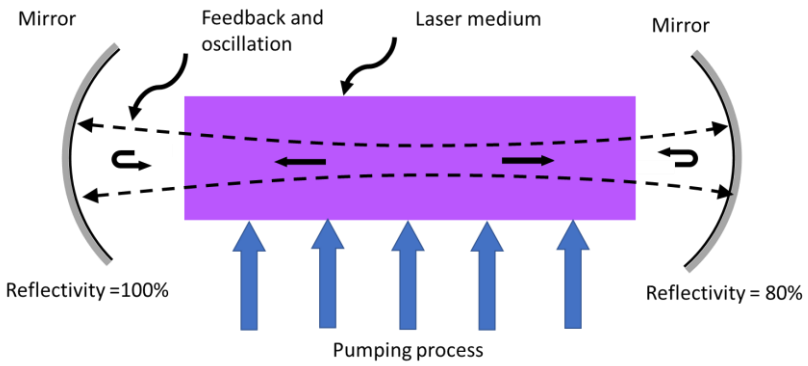

Figure 1.1. Schematic of laser

A typical laser oscillator is shown in Figure 1.1. It includes (i) a laser medium consisting of an appropriate collection of atoms, molecules, ions, or in some instances a semiconducting crystal; (ii) a pumping process to excite these atoms (molecules, etc.) into higher quantum-mechanical

energy levels; and (iii) suitable optical feedback elements that allow a beam of radiation to either pass through the laser medium (as in a laser amplifier) or bounce back and forth repeatedly through the laser medium (as in a laser oscillator)[1].

Many scientific, military, medical and commercial laser applications have been developed since the invention of laser. The coherency, high monochromaticity, and ability to reach extremely high powers are all properties which allow for these specialized applications.

1.2 Laser-induced plasmas and current challenges

1.2.1 Applications of laser-induced plasmas

Laser-induced plasmas have numerous research and industrial applications. These include studying nonequilibrium plasmas[2] and exploring various nonlinear effects at beam propagation such as laser pulse filamentation, laser beam collapse, self-trapping, dispersion, modulation instability, pulse splitting, and soft ionization in mass spectroscopy. [3-7]

Laser-plasma accelerators are another area of the laser-induced plasma application. The area originated in the 1980s and is associated with a high intensity ultrashort laser field separating the electrons from the ions in the plasma. As result an extreme high magnitude longitudinal electric field is generated in the wake of the laser which is able to accelerate light particles like electrons. The scale length of the Wakefield is the plasma scale wavelength 10-30 μm for plasma electron densities of $n_e = 10^{18} - 10^{19}\, cm^{-3}$. As a result multi-gigaelectron electron beams can be obtained. For example, a 200 TW, 30 fs laser can produce a 0.3 nC electron beam at 1.5 GeV over 1 cm length with a 3.8% energy spread and a 10 GeV, 1 nC beam can be obtained using a 2 PW, 100 fs laser over 15 cm length [8,9] This has resulted in development of X-ray and deep UV radiation sources.[10,11]

Finally, laser-induced plasma has been widely applied in diagnostic techniques such as laser-induced breakdown spectroscopy and laser electronic excitation tagging. More detailed information on these diagnostic methods can be found elsewhere.[6,12,13]

1.2.2 Nonlinear photoionization fundamentals

In the mid -1960's the scientific community began experimenting with lasers by placing a focusing lens in front of the beam. This resulted in electrical breakdown of the medium and creation of plasmas.[14,15,16] Keldysh in his seminal work presented the various regimes in which photoionization can take place.[14]

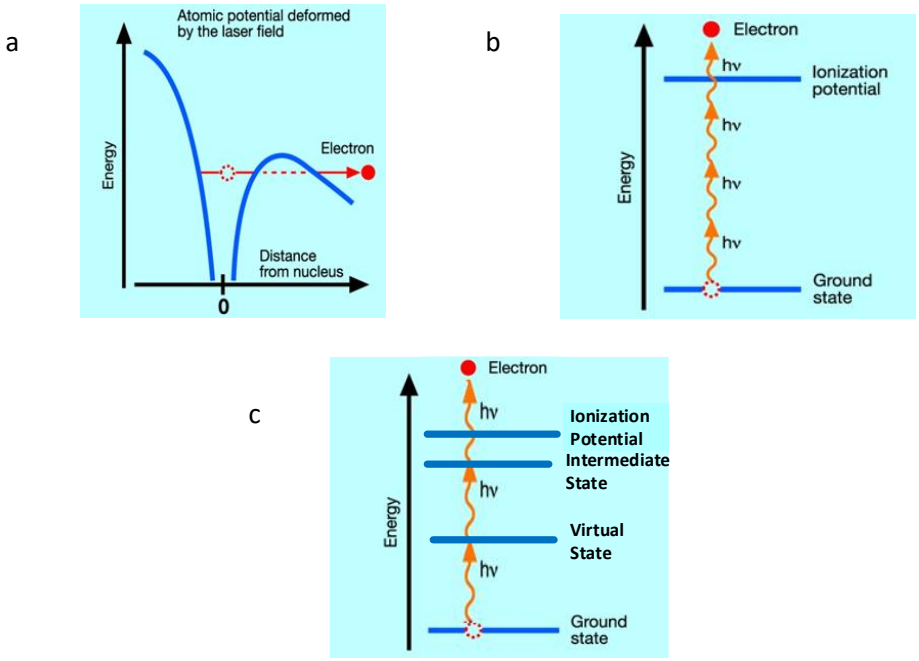

Figure 1.2. Nonlinear photoionization: (a) Tunneling ionization and (b) Multiphoton ionization (MPI) (c) 2+1 Resonance Enhanced Multiphoton Ionization process

The photoionization process is schematically illustrated in Figure 1.2. Photoionization is the physical process in which electromagnetic radiation is absorbed by atoms (or molecules) resulting in release of a bound electron into the continuum (ionization). The governing mechanism is

dictated by the Keldysh parameter γ, defined as the ratio of laser frequency ω to tunneling frequency ω_t (which characterizes the time of electron tunneling through the potential barrier) :

$$\gamma = \frac{\omega}{\omega_t} = \frac{\omega\sqrt{2m\mathcal{E}_i}}{eE} \qquad \text{Eq. 1.1}$$

where E- amplitude of incident electric field, $\mathcal{E}_i$- ionization potential, m and e are electron mass and charge respectively.

In the case of low frequency limit (and/or large laser intensity) $\omega \ll \omega_t$, the electron has sufficient time to tunnel through the barrier and ionization is driven by tunnelin, while for the high-frequency limit (and/or low laser intensity) $\omega \gg \omega_t$, the electric field varies faster than the time required for tunneling and ionization is governed by the Multi-Photon Ionization (MPI) process.

A special case of nonlinear multiphoton ionization is Resonance Enhanced Multi-Photon Ionization (REMPI). Keldysh[14] described that when electromagnetic radiation is tuned to a certain electronic transition of the atom or molecule the probability of ionization increases by orders of magnitude. The species first goes to the excited intermediate state and then into the continuum spectrum.

Specifically, in the *m*+*n* REMPI scheme, *m* photons are first simultaneously absorbed by an atom or molecule to bring it to an excited state. Other *n* photons are further absorbed which results in ionization and generation of an electron and ion pair. Figure 1.2(c) gives the example of a 2+1 REMPI process. Typically, a tunable laser is used to selectively ionize a species at its resonant wavelength.

REMPI using UV energies has been applied to monoatomic species such as *Ar* (3+1 REMPI at 226.3nm), *Xe, O* and *H* atoms or multiatomic species like *CO*, *NO* (2+1 REMPI $C^2\Pi - X$ at

190 nm), and NH_3. [7,17,18] In the case of *CO*, the ionization energy required is 14.01 eV. This will require an 88.4nm photon which lies in the extreme UV region of the electromagnetic spectrum. Thus a 2+1 mechanism is used using a 230nm photon via the $B^1\Sigma \leftarrow X^1\Sigma$, Hopfield– Birge system.

1.2.3 Challenges of laser-induced multiphoton ionization

The previous sections reviewed importance of Multi-Photon Ionization (MPI) as a fundamental first step in high-energy laser-matter interaction critical for understanding the mechanism of plasma formation. With the discovery of MPI more than 50 years ago, there were numerous attempts to determine basic physical constants of this process in the direct experiments, namely photoionization rates and cross-sections of the MPI; however, no reliable data is available even today and spread in the literature values often reaches 2-3 orders of magnitude. This is due to the inability to conduct absolute measurements of plasma electron numbers generated by MPI which leads to uncertainties and, sometimes, contradictions between the MPI cross-section values utilized by different researchers across the field and is elaborated upon in the following paragraphs.

The most prominent and developed diagnostic of laser-induced plasmas is laser interferometry. However, laser interferometry is limited to $n_e \sim 10^{16} - 10^{17}\ cm^{-3}$ due to the minimal measurable shifts of the interference fringes, while regime when nonlinear optical phenomena (self-focusing due to the Kerr effect and defocusing on generated plasma) can be neglected is associated with lower electron number densities $n_e \sim 10^{15} - 10^{16}\ cm^{-3}$.[19,20] Several semi-empirical methods for relative measurements of plasma density were also proposed; however, all of them require absolute calibration based upon theoretically predicted values of plasma number density. Time-of-flight (TOF) mass spectrometer measurements of ion currents generated by laser-induced plasma filament have been conducted to measure photoionization rates.[21-23] The fundamental limitation of

this technique is the inability to conduct absolute calibration of the system since the reference object (for example a box containing known quantity of electrons) against which the calibration can be completed is not readily available. Instead, the TOF mass spectrometer measurements relied on theoretically estimating the of total number of electrons in the focal zone to conduct absolute system calibration. Very recently, scattering of THz radiation from the laser-induced plasmas was proposed for spatially unresolved relative measurements of n_e.[24,25] Other measurement techniques were proposed recently based on measurements of capacitive response times of system including a capacitor coupled with laser-induced plasma loaded inside.[26,27] These attempts to measure n_e in laser-induced plasmas are characterized by various degrees of success and reliability of obtained data, but none of them currently provides the ultimate solution for absolute plasma density measurements.

Analysis of various theoretical and semi-empirical approaches undertaken previously led to large variability of photoionization process constants available in the literature and with some of them even controversial. For example, photoionization rates for O_2 reported by Mishima in Ref. [28] are approximately 2 orders of magnitude higher than that reported by Talebpour in Ref. [22]. In addition, photoionization rate for O_2 is three orders of magnitude higher compared to N_2,[28] while experimentally determined photoionization rates reported by Talebpour for N_2 and O_2 yields doubtful proximity, namely $1.5 \times 10^9\ s^{-1}$ for N_2 and $3 \times 10^9\ s^{-1}$ for O_2 for the laser intensity 3×10^{13} W/cm^2.[22]

1.3 Laser diagnostics of combustion: State-of-the-art, current challenges and potential of laser-induced plasmas

Lasers have increasingly been used for combustion system diagnostics. Various techniques have been developed to measure properties such as temperature, concentrations, and flow velocities. using lasers. Lasers offer a non-intrusive way for such measurements when compared to physical probes which are often difficult to implement due to difficulties in access and damage in harsh environments with high temperature and/or pressure. The ability to focus the laser beam into small probe size of 100s of microns to few millimeters allows spatially resolved measurements. The pulse duration (ns-fs) and repetition frequency (in the MHz) of the laser permit time resolved measurements of the various combustion parameters.[29,30,31,32]

Following description in this section will focus specifically on carbon monoxide (*CO*) diagnostics in combustion. Carbon monoxide is an important intermediate in combustion chemistry of carbon-based that is generated as a result of incomplete combustion and impacts soot formation.[33] It might be harmful to the environment as it contributes to the greenhouse gas levels in the atmosphere and is directly hazardous to living beings at concentrations >27 ppm.[34,35] Therefore, it is essential to accurately monitor *CO* concentration in gaseous mixtures at combustion.

Traditionally, optical techniques have been used for diagnostics of *CO* in combustion. Absorption spectroscopy such as Tunable Laser Absorption Spectroscopy (TLAS) and Infrared Absorption Spectroscopy (IAS) provides high sensitivity while lacking spatial resolution due to the involved averaging over laser propagation path. These techniques have been used extensively for in-situ *CO* measurements in various kinds of hydrocarbon flames. Concentration and te3mperature measurements have been reported in atmospheric pressure methane-air, ethylene-air,

flat-burner laminar and diffusion flames as well as rotary kiln and coal burners. However, large acquisition times from 1s up to 30s and path averaging are necessary to achieve desired measurement sensitivity. [11,36-39]

Another popular diagnostic is Coherent Anti-Stokes Raman Spectroscopy (CARS), which utilizes a non-linear 4 wave mixing process. CARS offers high sensitivity measurements of temperature, pressure, species density, and relative concentration. However, being a non-linear process, it requires overlap of multiple beams in temporal and spatial domain. Such strict requirements lead to great experimental complexities.[40-43]

Laser-Induced Fluorescence (LIF) is a powerful technique which proved spatial resolution and selectivity and has been used in measuring gaseous species in flames.[44] However, electronic resonant states utilized for *CO* excitation are located in the vacuum ultraviolet (VUV) spectral region, which is absorbed by the atmospheric air. This reason rules out a resonant state excitation based on absorption of a single photon. Instead, species may be excited by two-photon absorption as successfully applied previously in Two-Photon Laser-Induced Fluorescence (TP-LIF) measurements in *CO*, NH_3, *O*, and *H* .[45-51]

TP-LIF of *CO* is especially challenging in high pressure combustion, which refers to the increase of the collisional quenching rate causing loss of the LIF signal.[47,48] Increasing of the laser intensity to recover the LIF signal was found to be not practical because it ionized the resonantly-excited *CO* molecules further augmenting the loss of fluorescence. Specifically, several previous studies reported a decreased LIF signal and a corresponding increase of photoionization in the probing region of the focusing beam, and an increased LIF signal l away from the focal region where the ionization was less severe.[45-48]

Utilization of fs-lasers for TP-LIF of *CO* at elevated pressures is advantageous, but does not resolve the problem of the fluorescence loss. Indeed, fs TP-LIF eliminates photodissociation-driven contamination of the emission spectra, avoids challenges associated with pressure-dependent absorption line broadening/shifting when narrowband lasers are used, and enables utilization of modest energies in the fs-laser pulse.[52,53] Recent studies evaluated the potential of fs TP-LIF to measure *CO* in a CH_4-air flat-burner flame up to 5 atm and in a CO/N_2 mixture up to 20 bars.[17,48] The fluorescence decreased dramatically with increasing pressure (up to 90% with pressure increase from 1 to 20 bar) was reported, and microewave scattering technique verified the presence of photoionized electrons in the probing region created by 2+1 REMPI process.[48]

Therefore, significant photoionization occurred in fs TP-LIF of *CO* at elevated pressures because they use higher laser pulse energies and peak power to overcome the loss of LIF signals discussed above. This photoionization generated in 2+1 REMPI process might create problem for LIF measurements, but, at the same time, it creates potential opportunity for the novel diagnostics methods based on measurements of the photoionized electrons directly. Such a method will be developed and tested in this work in Chapter 4.

1.4 Microwave scattering for diagnostics of microplasmas

Development of miniature plasmas and microdischarges, including laser-induced plasmas, non-equilibrium atmospheric pressure plasma jets, nanosecond repetitive pulsed discharges in air, requires designing of appropriate plasma diagnostic techniques. Conventional diagnostics cannot be applied to these microplasmas. Microwave interferometry fails due to diffraction and small phase shift acquired when propagating through a small sized plasma. Laser Thomson scattering often cannot be applied since discharges are highly unsteady and the long accumulation of the

signal required to achieve measurable signal levels is not feasible.

The concept of microwave scattering technique for microplasma diagnostics was first proposed theoretically by Shneider[54] and was then successfully implemented in a number of relative measurements of laser-induced avalanche ionization in air, resonance-enhanced multiphoton ionization in argon, and atmospheric pressure plasma jets.[21,54-57]Absolute measurements of the electron plasma density by using microwave scattering was proposed by Shashurin and demonstrated with several plasma objects including non-equilibrium atmospheric pressure plasma jets, microdischarges used for electrosurgery, and nanosecond repetitive pulsed discharges in air.[56-64]

Conceptually this approach involves scattering the microwave radiation off the plasma volume in the quasi-Rayleigh regime (denoted as RMS in the following description), when the prolonged plasma volume is oriented along the linearly polarized microwaves and the plasma diameter is small compared to the spatial scale of the microwave field so that the incident microwave electric field is distributed uniformly across the entire plasma volume. ("Quasi" is used to identify that scattering is equivalent to classical Rayleigh scattering if incident radiation is linearly polarized along the lengthened direction of the plasma object.) In this case, the plasma electrons experience coherent oscillations in the incident microwave field and radiate a Hertzian dipole radiation pattern in a far field. Overall, such a process is analogous to elastic Rayleigh scattering of light, when radiation wavelength significantly exceeds the scatterer size. Signal scattered from the plasma is proportional to the total electron numbers in the plasma volume. Absolute calibration of the RMS system can be conducted using dielectric scatterers with known physical properties. Measuring the scattered signal amplitude allows determining the total number of electrons in the plasma volume and average plasma density after appropriately calibrating the system with dielectric scatterers.

Let us now consider fundamentals of the RMS technique in more detail. We limit the following description to one specific plasma geometry, namely, a slender prolate plasma channel with length (l) significantly exceeding the diameter (d) oriented along the incident microwave field.

We first demonstrate that in conditions of current study the amplitude of the electric field induced inside the scatterer channel as a result of irradiation with microwaves is uniform throughout the channel and equal to the field amplitude E_i in the incident wave. For conditions of the current study, the plasma channel can be considered thin compared to skin layer depth (so that $f[GHz] \leq \frac{2.5}{\sigma[\Omega^{-1}cm^{-1}]\cdot d[mm]^2}$). [65] In this case, the amplitude of the electric field induced inside the scatterer with dielectric permittivity ε and conductivity σ can be written as $E = \frac{E_i}{\sqrt{(1+k(\varepsilon-1))^2+\left(k\frac{\sigma}{\varepsilon_0\omega}\right)^2}}$, where k is the depolarization factor governed by the channel geometry and E_i is the amplitude of incident microwave electric field at the channel location. [62,66,67] For experimental conditions in this study, the large aspect ratio $AR=l/d>>1$ makes the depolarization factor $k\approx\frac{1}{AR^2}\ln(AR)<<1$. [62,65,66] Therefore, the amplitude of the electric field inside the channel is close to that in the incident wave $E = E_i$. [66, 68] Flatness of the wave front surface along the scatterer length is ensured by placing the plasma scatterer at distance $r > \frac{l^2}{\lambda} \approx 1$ cm.

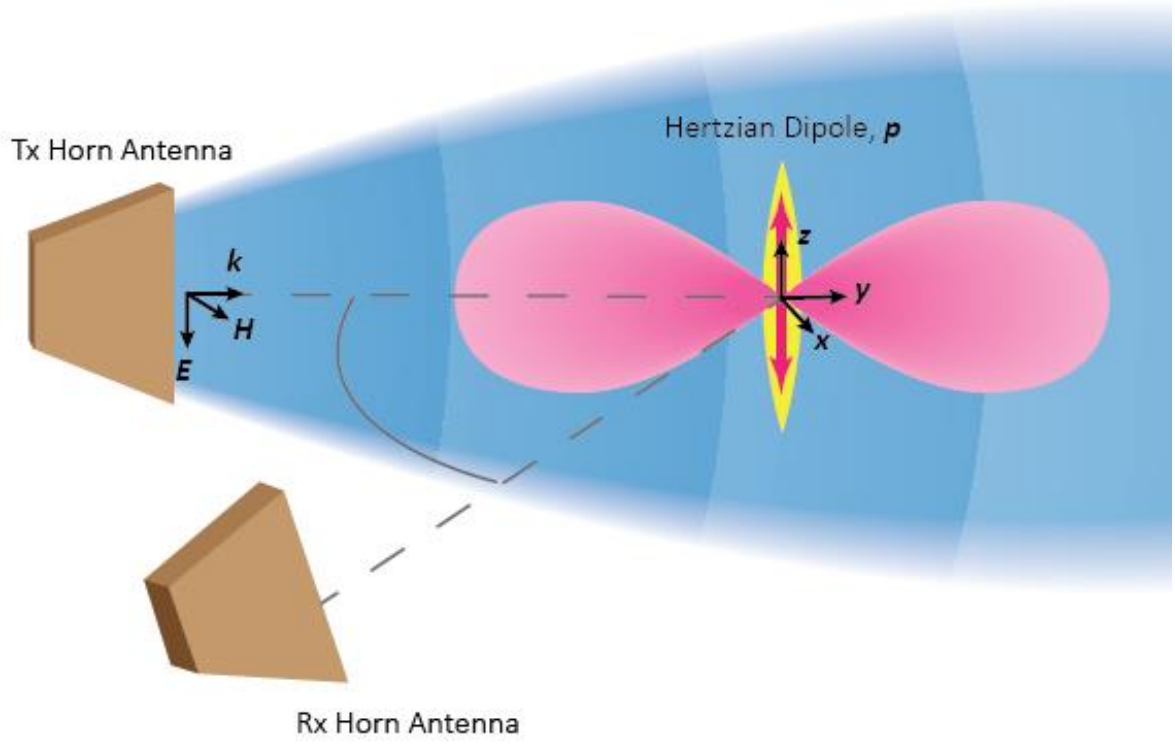

Figure 1.3. Detailed schematic of the Rayleigh Microwave Scattering (RMS) technique

Electrons in the plasma volume experience oscillations with amplitude of $s = \frac{eE_i}{m\nu\omega}$ due to the incident microwave field (we consider no restoring force due prolate plasma channel geometries)[54]. Electron collision frequency in the denominator is governed by those with gas particles (ν_{eg}) for densities <10^{17} cm^{-3}, since the contribution of electron-ion collisions may be neglected in that range, so $s = \frac{eE_i}{m\nu_{eg}\omega}$. Electron-gas collision frequency ν_{eg} is independent of plasma density ensuring that electrons in each location inside the plasma volume experience

essentially same displacement ($\nu_{eg} = 5.18 \times 10^{11}$ s^{-1} based on electron-gas elastic collision cross-section $\sigma_{eg} = 5 \times 10^{-16}$ cm^{-2} and electron temperature T_e=0.4 eV).[65,27]

Total dipole moment of the plasma channel (p) is given by:

$$p = es \int n(r,z) 2\pi r dr dz = esN_e = \frac{e^2}{m\nu}\frac{E_i}{\omega}N_e \qquad \text{Eq. 1.2}$$

Radiation from the plasma dipole in the plane perpendicular to the dipole orientation is detected by the same horn antenna as incident one (see Figure 1.3). The antenna is placed at distance r =6 cm from the plasma channel to ensure that the dominant contribution of far-field $\left(\sim\frac{k^2p}{r}\right)$, while near-field $\left(\sim\frac{p}{r^3}\right)$ is negligible (kr >6).[69] Thus, the amplitude of the electric field at location of the detecting horn is

$$E_s = \frac{k^2p}{r} = \frac{e^2}{mc^2\nu}\frac{\omega E_i}{r}N_e \qquad \text{Eq. 1.3}$$

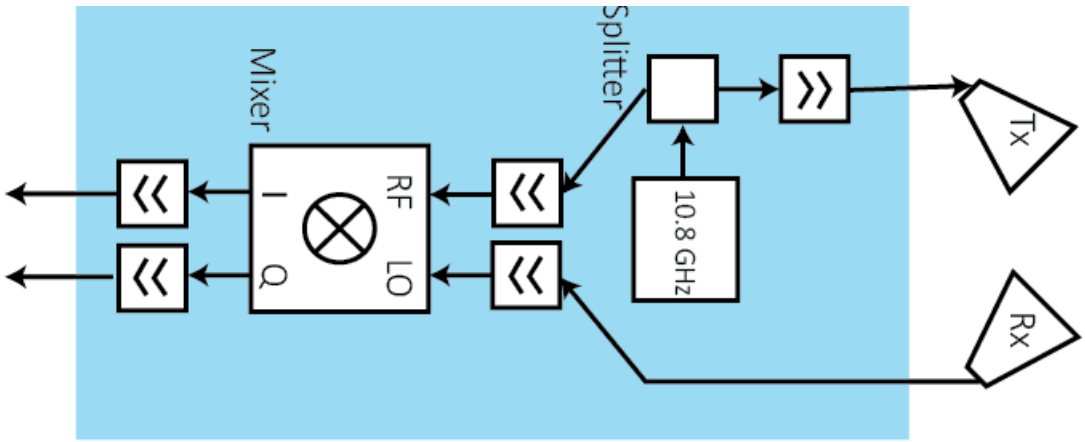

Figure 1.4. Homodyne detection system

A homodyne-type detection system schematically shown in Figure 1.4 is typically used for the scattered microwave signal measurements which provides output voltage $U_{out} \propto E_s$. The detection was achieved by means an of *I/Q* Mixer, providing in-phase (*I*) and quadrature (*Q*) outputs. The total amplitude of the scattered microwave signal is determined by $U_{out} = \sqrt{I^2 + Q^2}$. The amplifiers and the mixer used in the microwave system are operating in a linear mode for the entire range of the scattered signal amplitudes, thereby ensuring that the output signal U_{out} is proportional to the electric field amplitude of scattered radiation E_s at the detection horn location, yielding

$$U_{out} \propto E_s = \frac{e^2}{mc^2 \nu} \frac{\omega E_i}{r} N_e \qquad \text{Eq. 1.4}$$

One can see that RMS system detects total number of electrons in plasma volume accurate to calibration constant *A* of specific microwave system used. Absolute calibration of the RMS can be conducted using dielectric scatterers with known physical properties. To this end, now we consider RMS system signal generated by the prolate scatterer made of dielectric material with dielectric constant ε and volume V. The only difference from the assessment above for the plasma channel would be that total dipole moment induced in the scatterer is $p = \varepsilon_0(\varepsilon - 1)E_i V$, and thus

$$U_{out} \propto E_s = \frac{\varepsilon_0(\varepsilon - 1)}{c^2} \frac{\omega^2 E_i}{r} V \qquad \text{Eq. 1.5}$$

One particularly convenient form of expression for measured output of RMS system is:

$$U_{out} = \begin{cases} A \cdot \frac{e^2}{m\nu} N_e & - \text{ for plasma} \\ A \cdot V \cdot \varepsilon_0 (\varepsilon - 1)\omega & - \text{ for dielectric bullet} \end{cases} \qquad \text{Eq. 1.6}$$

where *A* –proportionality coefficient which is a property of the specific microwave system (utilized components, geometry, microwave power, etc.) while independent of scatterer properties and it can be found using scatterers with known properties. Lower Eq. is used for calibration of specific microwave system, namely to determine value of coefficient *A*. Cylindrical dielectric bullets with diameter 3.175 mm and length 1 cm made of Teflon are typically used. The bullets are shot through the microwave field (along the same axis where plasma was placed later) using pneumatic gun with velocities below 100 m/s to generate time-varying response on the dielectric bullet passage for separation of signal scattered from the bullet from one DC background caused by reflections from surroundings, elements of microwave circuit etc. Typical calibration signal generated by Teflon bullet is shown in Figure 1.5.

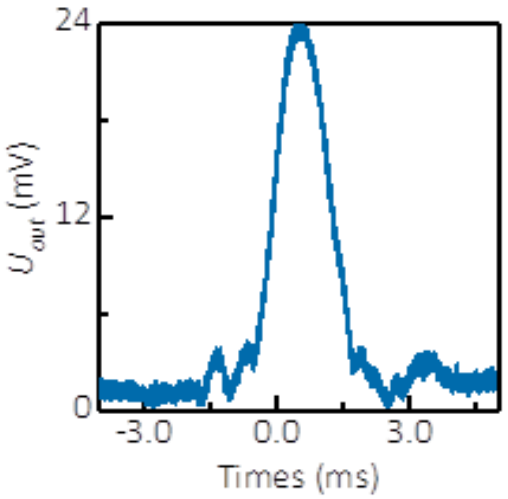

Figure 1.5. Calibration of the of the Rayleigh Microwave Scattering (RMS) system

Microwave scattering is effective for microplasma diagnostics. The electrons number $10^8 - 10^{12}$ have been measured in previous experiments in plasma objects such as APPJ, pin-to-pin nanosecond repetitively pulsed discharges.[63,59] Thus, MS also has high potential as a toll for diagnostics of laser induced plasmas.

1.5 Motivation

The first motivation of this work was to study fundamental properties of the MPI process. As emphasized in the previous sections the MPI rates and cross sections are largely unknown even 50 year after the discovery. Large discrepancy in photoionization rates available in the literature causes sometimes contradictory conclusions and generally disadvantageous for wide class of problems involving laser-induced plasmas. At the same time, recent development of RMS technique for diagnostics of micro-plasma demonstrated potential to measure electron numbers produced by MPI and subsequently determine ionization rates and cross-sections of MPI for different gases in direct experiment. Direct measurements of the absolute electron numbers in laser-induced plasma are highly sought in the high directed energy applications, virtual ultra-fast reconfigurable antennae systems for radiating and redirecting of electromagnetic power, cavity free lasing sources, drag reduction applications for hypersonics, lightning protection, laser methods in material processing, laser plasma diagnostic techniques, combustion diagnostics, and plasma-assisted combustion etc. Also, tabulation of MPI cross-sections and photoionization rates for variety of gases has great importance for computational efforts concerned with modeling of laser-induced plasmas.

The second motivation was to use REMPI in combination with RMS for diagnostics in combustion systems. As emphasized in previous sections detection and measurement of

concentration of species (e.g. *CO*) is important and currently very challenging at high pressure combustion systems. The challenge refers to the loss of the LIF signal and production of substantial photoionization in 2+1 REMPI process. The same ionization, however, provides a unique opportunity to use the RMS technique for detection of photoelectrons and potential to create REMPI-RMS-based diagnostic technique for high pressure combustion.

1.6 Objectives

The objectives can be divided into two parts. The first part is aimed at studying the phenomenon of MPI in various gases. The general objective is to determine the fundamental constants of the photoionization process which are currently largely unknown and study plasma dynamics. Our initial goal is to measure the number of generated by an 800 nm fs-laser pulse for various laser intensities by RMS technique. The next goal is to use these measurements to determine the cross-section of multiphoton ionization and photoionization rates for various gases of practical importance (such as O_2, *Xe*, *Ar*, N_2, *Kr* and *CO)* and a broad range of laser pulse energies. Finally, validation of the measured plasma decay dynamics in the wake of fs-laser-induced spark against the 1D axially symmetric model developed by Dr. M. N. Shneider is targeted.

The second part of this work is aimed to develop a practical application of REMPI-RMS system for combustion diagnostics. Specifically, measurements of *CO* number density in gaseous mixtures are targeted. In REMPI-RMS technique, a tunable laser is used to selectively ionize *CO* molecules via 2+1 REMPI process at 230.1 nm, and then plasma electrons are subsequently detected by the RMS method. Our first goal is to explore the capability of REMPI-RMS diagnostic technique for detecting *CO* in the nitrogen buffer in a single spatial location in atmospheric and at

elevated pressures. Subsequent goal is to demonstrate the feasibility of spatially resolved measurements by creating multiple MPI sites and subsequent measurement by the RMS technique.

1.7 Outline

In Chapter 2, RMS measurements of laser-induced plasma generated by 800 nm fs-laser pulse in air and methodology for determination of MPI cross sections and photoionization rates are presented. The use of RMS technique to measure the total number of electrons and electron number density is described. Plasma decay after the fs-laser pulse is presented and compared with results simulated by Dr. M. N. Shneider using a 1D axially symmetric model of laser spark.

In Chapter 3, photoionization rates of various monoatomic and diatomic gases including *Ar, Kr, Xe, O_2, N_2, CO* by 800 nm photons are determined based on electron number measurements conducted by RMS technique and following methodology developed in Chapter 2. Plasma decay in the wake of the fs-laser pulse is presented and analysed.

In Chapter 4, REMPI-RMS diagnostics of carbon monoxide in nitrogen buffer at elevated pressures is presented and used for measuring *CO* number densities. A four (4) energy level model of *CO* molecule is presented and used to analyze the experimental findings. The scaling laws for the number of REMPI-generated electrons and LIF signal with *CO* number density and laser pulse energy are discussed and the limits for the applicability of REMPI-RMS diagnostics are evaluated.

Chapter 5 presents conclusions and recommendations for future work.

2. FS-LASER-INDUCED MULTIPHOTON IONIZATION IN AIR

Modified from Paper published in *Sci Rep* **8,** 2874 (2018).
Animesh Sharma, Mikhail. N. Slipchenko, Mikhail. N. Shneider, Xingxing. Wang, K. Arafat Rahman & Alexey Shashurin

2.1 Methodology of MPI cross-section determination

Ionization of gas by intense fs-laser pulse is associated with multiphoton and tunneling processes, which are two limiting cases of essentially same physical process of nonlinear photoionization. Choice of the governing mechanism is dictated by Keldysh parameter γ, defined as a ratio of laser frequency ω to tunneling frequency ω_t characterizing time of electron tunneling through the potential barrier: $\gamma = \frac{\omega}{\omega_t} = \frac{\omega\sqrt{2m\mathcal{E}_i}}{eE}$, where E- amplitude of incident electric field, $\mathcal{E}_i$- ionization potential, m and e are electron mass and charge respectively. In the case of low frequency limit (and/or large laser intensity) $\omega < \omega_t$, the electron has sufficient time to tunnel through the barrier and ionization is driven tunneling effect, while the high-frequency limit (and/or low laser intensity) $\omega > \omega_t$, the electric field varie faster than the time required for tunneling and ionization is governed by the MPI process.

Our method determined the cross-seciton of the MPI based on an absolute measurements of total electron numebr (N_e) generated by a femtosecond (fs) laser pulse and precise measurements of the laser pulse characteristics. The experiments have been conducted at low laser intensities ($\leq 10^{13}$ W/cm^2 as detailed below) to ensure pure linear operation regime when nonlinearities associated with plasma creation and the optical Kerr effect are negligible. In this case plasma

formation due to MPI by the femtosecond laser is described by simple differential equation $\frac{\partial n_e}{\partial t} = \nu \cdot (n_0 - n_e)$, where n_e is the plasma density, $\nu = \sigma_m I^m$ – is the local ionization rate, σ_m – cross-section of m-photon ionization process with $m = \mathrm{Int}\left(\frac{\mathcal{E}_i}{\hbar\omega}\right) + 1$, I– local instantaneous value of laser field intensity, and n_0 is background gas density, while other physical processes can be neglected on the short time scale of the laser pulse.[70] This equation can be easily integrated and plasma density n_e created as result of the femtosecond laser pulse is $n_e = n_0\left(1 - e^{-\int \nu dt}\right)$. a low ionization degree $n_e \ll n_0$ the plasma density distribution immediately after the laser pulse is

$$n_e(\mathbf{r}) = n_0 \int \nu dt = \sigma_m n_0 \int I(\mathbf{r}, t)^m dt \qquad \text{Eq. 2.1}$$

where time integration is taken over the duration of the laser pulse at particular location **r**. The total electron number N_e generated by the laser pulse is obtained by integrating Eq. 2.1 over the entire plasma volume to obtain

$$N_e = \sigma_m n_0 \int \int I(\mathbf{r}, t)^m dt dV \qquad \text{Eq. 2.2}$$

Eq. 2.2 provides general a expression that can be used to determine the MPI cross-section as follows. Total electron numbers (N_e) generated by the femtosecond laser pulse are measured using the Rayleigh Microwave Scattering (RMS) technique. Spatial and temporal intensity distribution $I(\mathbf{r}, t)$ is determined in precise measurements of laser beam and integral on the right hand side can be calculated. Then, one can determine σ_m from the Eq. 2.2 for the known background gas density n_0.

The general expression Eq. 2.2 can be simplified by making additional assumptions Firstly, we will consider the most practical case a of Gaussian beam. In this case, spatial and temporal intensity dependences can be expressed as

$$I(r,z,t) = I_0 \frac{w_0^2}{w(z)^2} e^{-\frac{2r^2}{w(z)^2}} e^{-\frac{(t-t^*)^2}{\tau^2}} \quad \text{Eq. 2.3}$$

where I_0 is the intensity in the beam center, w_0 is the $1/e^2$ waist radius (at z=0), $w(z) = w_0\sqrt{1+\left(\frac{z}{z_R}\right)^2}$ – $1/e^2$ beam radius at location z along the beam, z_R is the Rayleigh length and τ is the characteristic temporal width of the beam. This approximation uses the standard non-dispersing medium Gaussian beam optics spatial distribution ($I_{\mathbf{r}}(r,z) = I_0 \frac{w_0^2}{w(z)^2} e^{-\frac{2r^2}{w(z)^2}}$) with Gaussian temporal shape $e^{-\frac{(t-t^*(r,z))^2}{\tau^2}}$, where $t^* = t^*(r,z)$ indicates the time when the beam reaches a particular (r,z)-location (it is taken that beam peak reaches the waist at z=0 at time t=0, so that $t^*(r,0) = 0$ and $t^*(0,z) = z/c$).[71] All parameters of the beam in Eq. 2.3, namely I_0, w_0, z_R and τ are determined experimentally.

Secondly, we will consider the case of atmospheric air and 800 nm laser. In this case, MPI of oxygen molecules is dominant process since O_2 photoionization rate is 2-3 order larger than that for N_2 due to its lower ionization potential.[22,28] Thus, using ionization energy of oxygen molecule $\mathcal{E}_i$=12.2 eV and energy of 800 nm ionizing photons of $\hbar\omega$ =1.55 eV, one can see that eight-photon photoionization process should be considered, namely m=8.

A simplified form of the expression Eq. 2.2 for MPI of air with a femtosecond laser pulse of Gaussian shape in temporal and spatial domains can now be deduced by analytical integration of

the intensity in the form (Eq. 2.3), namely: $\int\int I(r,z,t)^8 dVdt = \frac{231\pi}{1024\cdot 16}\sqrt{\frac{\pi}{8}} {I_0}^8 \pi w_0^2 z_R \tau$ (see Appendix I) and substituting it into the right-hand side of the Eq. 2.2. Finally, Eq. 2.2 can be reduced to the form:

$$N_e = \frac{231\pi}{1024 \cdot 16}\sqrt{\frac{\pi}{8}}\sigma_8 n_0 \tau \pi w_0^2 z_R \cdot {I_0}^8 \qquad \text{Eq. 2.4}$$

The determination of MPI cross-section of oxygen is conducted using Eq. 2.4 as follows. N_e in the left-hand side of the equation is measured using the RMS system. Spatial and temporal characteristics of the laser beam (I_0, w_0, z_R and τ) in the right-hand side of the Eq. 2.4 are measured directly. Then, experimental dependence of N_e vs. laser intensities I_0 is plotted and σ_8 is determined by obtaining the best fit of that dependence using Eq. 2.4.

2.2 Experimental Details

The experimental layout including femtosecond laser and RMS system are shown schematically in Figure 2.1. Photoionization of air (relative humidity 30%, temperature about 300 K) was achieved by focusing laser pulses having Gaussian temporal and spatial shape from a 800 nm Ti:Sapphire laser of 164 fs FWHM having repetition rate of 100 Hz using a 1000 mm plano-convex lens. The laser repetition rate was decreased from nominal 1 kHz to ensure no memory effect in the interrogated volume. Diameter of incident beam on the lens was 7 mm. The pulse energy was varied using a linear polarizer and measured using laser power meter (Gentec-EO XLP12-3S-H2-DO). Images of the plasma were taken using 1024i Pi Max 4 ICCD camera. Coordinate z=0 was chosen at the beam focal plane of the strongly attenuated laser beam (no plasma presents).

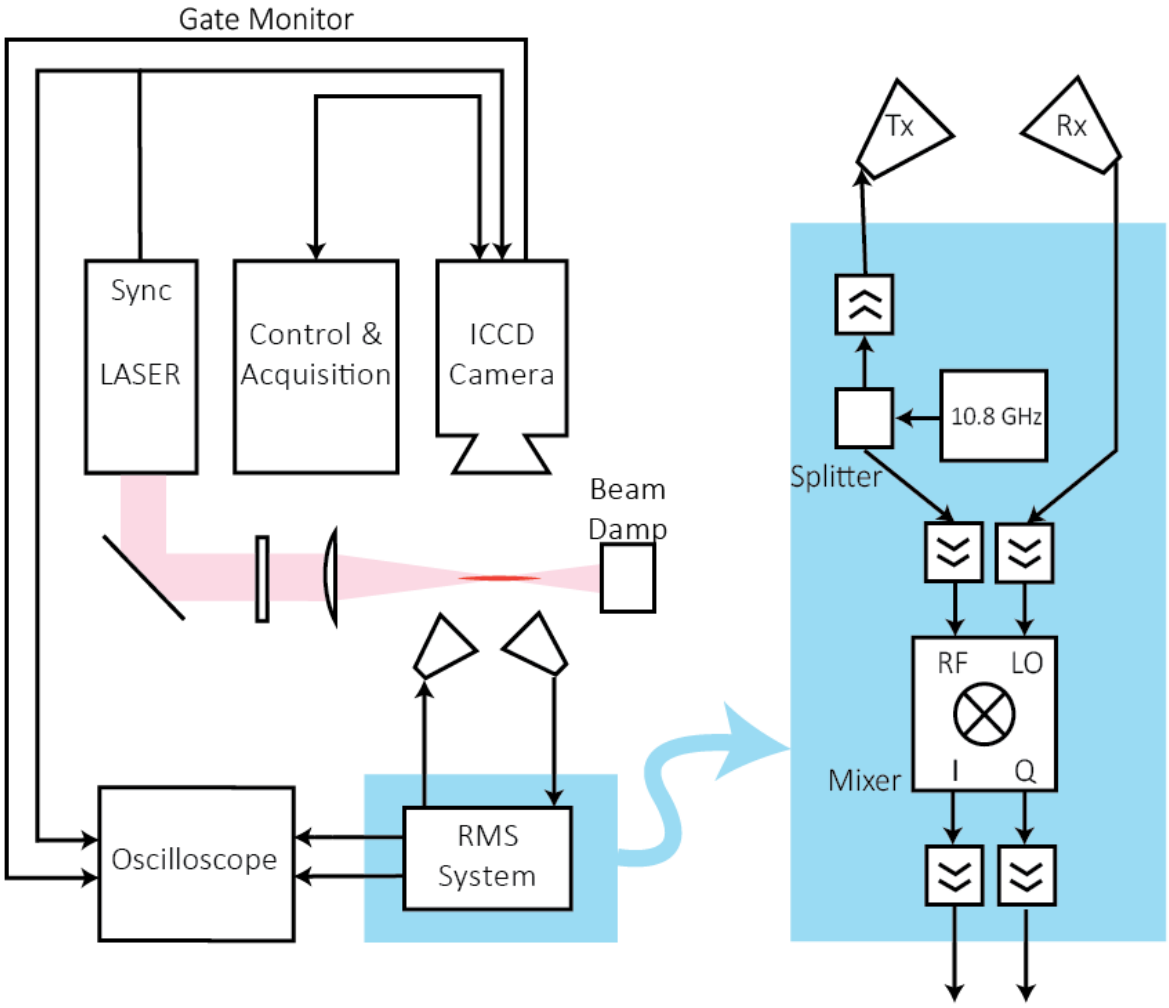

Figure 2.1. Experimental setup and RMS homodyne detection system. A 800 nm Ti:Sapphire femtosecond laser operating at repetition rate of 100 Hz was focused using a 1000 mm plano-convex lens to create the plasma. Homodyne-type Rayleigh microwave scattering system calibrated against dielectric scatterers was used to measure absolute number of electrons in the plasma volume.

Photograph of the fs-laser system used in the experiments and it main components is shown in Figure 2.2.

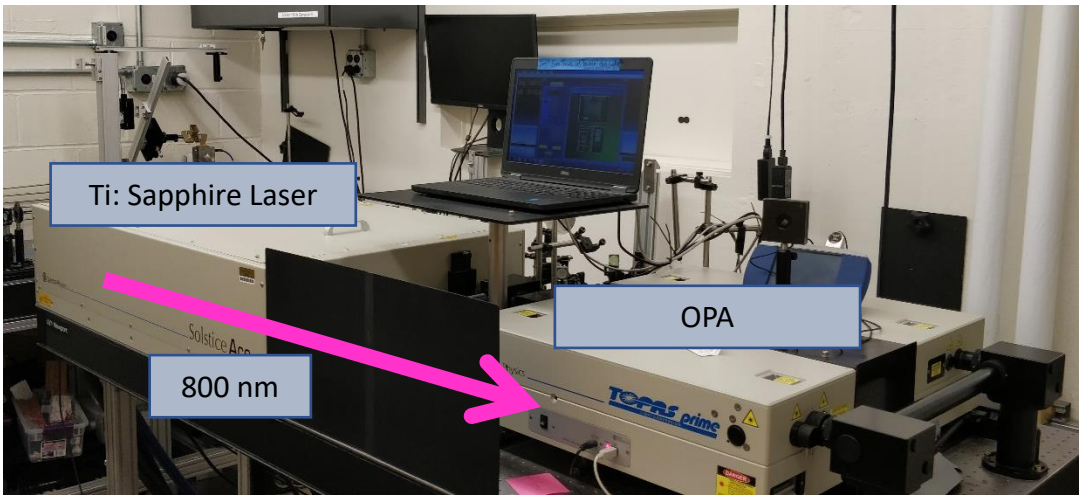

Figure 2.2. Femtosecond laser system used in the experiments

Measurements of the total number of electrons in the plasma volume were conducted using Rayleigh Microwave Scattering (RMS) diagnostics. Homodyne-type RMS system operating at the microwave frequency 10.8 GHz was used as shown schematically in Figure 2.1. The microwave signal from the source was splitted in two arms: one arm sent microwaves to the plasma using radiating horn, while second arm delivered the signal directly to LO-input of the *I/Q* mixer. Microwave radiation was linearly polarized along the plasma channel orientation. Radiating and detecting horns were mounted at the distance 6 cm from the plasma. The signal scattered from the plasma was received by the detecting horn, amplified and sent to the RF-input of *I/Q* mixer. The two outputs of the *I/Q* mixer were again amplified and captured on the oscilloscope. All components of the microwave system operated in the linear range of powers to ensure the measured response proportional to the amplitude of signal scattered from the plasma volume. The overall time response of the system was measured to be about 250 ps.

Typical photographs of individual fs-laser-induced plasma event taken at 100, 400 and 700 ns after the laser pulse by ICCD camera with 5 ns exposure time are shown in Figure 2.3.

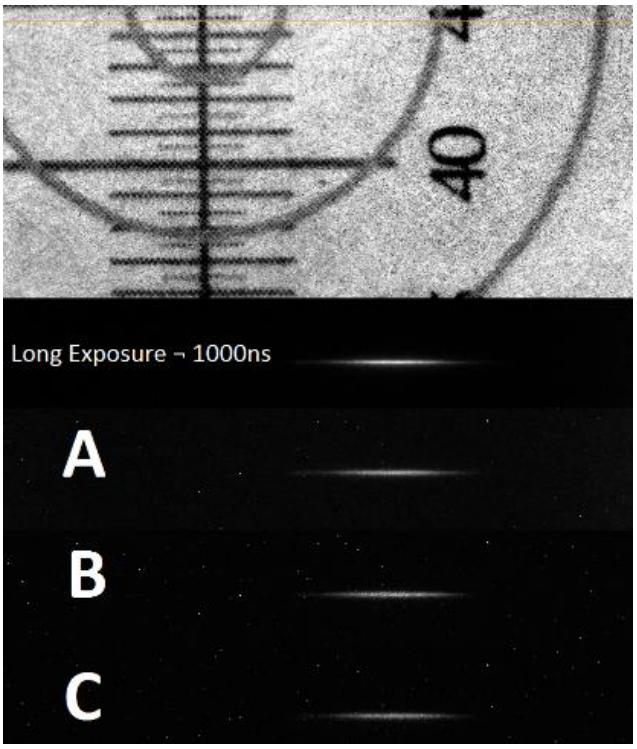

Figure 2.3. Typical photographs of individual fs-laser-induced plasma event taken by ICCD camera at different moments of time after the laser pulse. A: 100 ns, B: 400ns, C: 700 ns. Exposure time 5 ns.

2.3 Measurements of MPI cross-section of oxygen

Spatial distribution of laser beam intensity was determined using beam profiler measurements conducted with a strongly attenuated laser beam. To this end, set of attenuator plates was used that reduced beam intensity manifold (about 2-3 orders of magnitude) to completely eliminate plasma creation.

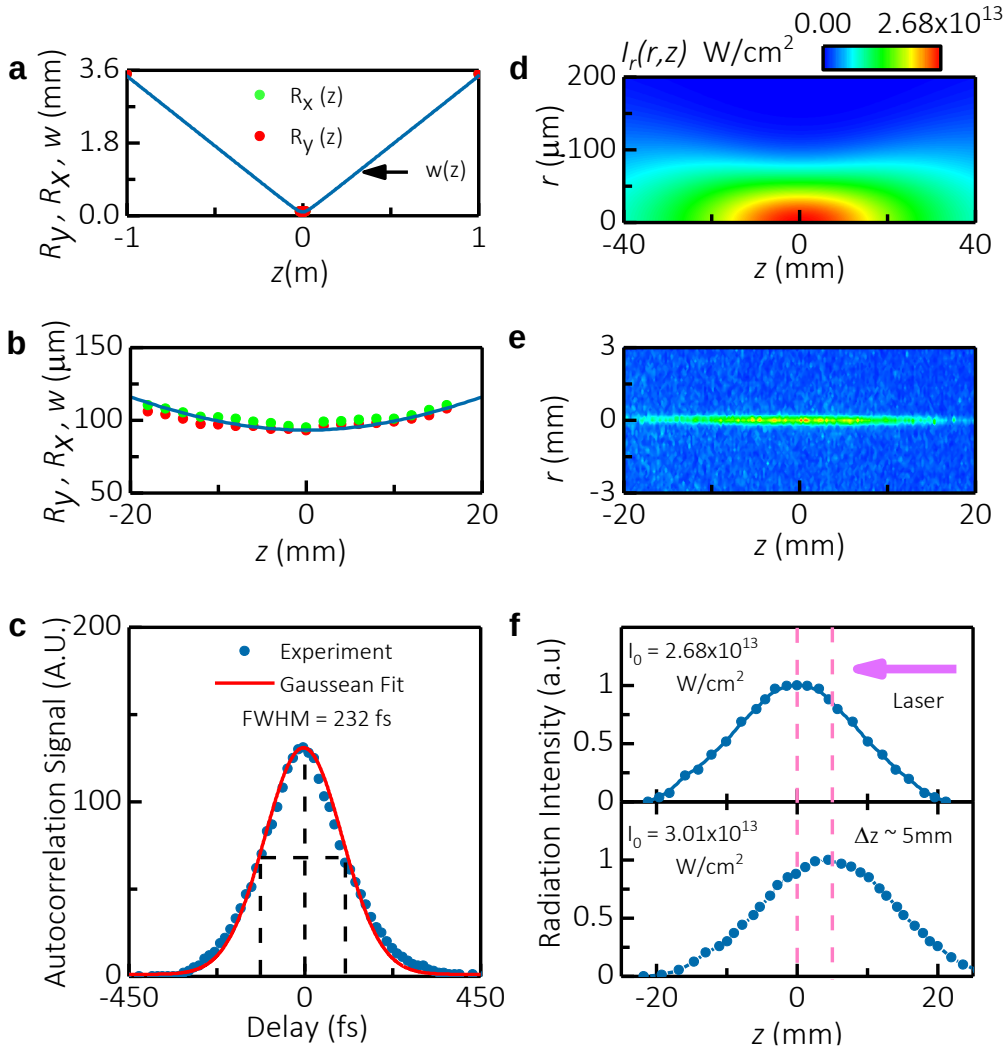

Figure 2.4. Measurements of the laser beam properties for intensity in the center I_0=2.68 x 10^{13} W/cm^2. (a-b) $1/e^2$ radius of the laser beam at various z-locations. (c) Intensity autocorrelation function approximated by the Gaussian fit. (d) 2D spatial distribution of the laser beam intensity approximated by Gaussian fit $I_r(r,z) = I_0 \frac{w_0^2}{w(z)^2} e^{-\frac{2r^2}{w(z)^2}}$ based on measured laser beam radius and Rayleigh length. (e) Photographs of laser-induced plasma taken at exposure time of 10 ns by ICCD camera. (f) Distribution of intensity radiated by the plasma plotted along the z-axis for two laser intensities.

$1/e^2$ radius of the beam measured using beam profiler at various z-locations is shown in Figure 2.4(a-b). Location of beam waist refers to coordinate z =0. Waist radius of in x - and y -directions

were R_x=92.17 μm and R_y=94.41 μm respectively. Average radius of the beam (w) was chosen to satisfy condition $\pi w^2 = \pi R_x R_y$ at each measured z -locations and was approximated by analytical function $w(z) = w_0\sqrt{1+\left(\frac{z}{z_R}\right)^2}$ with waist radius w_0=93.28 μm and Rayleigh length z_R=26.98 mm to achieve the best fit of the experimental data.

Temporal shape of the laser pulse was determined using measurements of intensity autocorrelation function by means of 2nd harmonic generation crystal. The autocorrelation function had nearly Gaussian shape with full width at half maximum (FWHM) equal to $FWHM_\tau = 232$ fs as shown in Figure 2.4(c). Thus, it was concluded that laser intensity in the time domain was also Gaussian with $FWHM_t = \frac{232\text{ fs}}{\sqrt{2}} = 164$ fs. Finally, temporal dependence of the laser intensity was approximated by Gaussian distribution $I \propto e^{-\frac{t^2}{\tau^2}}$ with $\tau = \frac{FWHM_t}{2\sqrt{\ln 2}}$= 98.6 fs.

Measured temporal and spatial parameters of the femtosecond laser pulse utilized in this work are summarized in the Table 1. Mean values averaged over the multiple measurements of the corresponding quantities and their standard errors are shown in the Table .

Table 2.1. Measured time-space parameters of the laser pulse

w_0	$1/e^2$ waist radius	93.28±0.66 μm
z_R	Rayleigh length	26.98±0.33 mm
τ	Temporal width	98.6±5.15 fs

Optical images of the laser-induced plasma created by MPI of air were analyzed to demonstrate that nonlinear effects in the non-attenuated laser beam were small and, thus, intensity

approximation used in Eq. 2.3 *Eq.* still applies when the plasma was on. Typical photograph of the laser-induced plasma taken by ICCD camera (exposure time *t*=0-10 ns) is shown in Figure 2.4(e) (energy in pulse 620 μJ, intensity at the beam center $I_0 = 2.68 \times 10^{13}$ W/cm^2). Figure 2.4 (f) shows corresponding distribution of plasma radiation intensity along z –axis for two laser intensities $I_0 = 2.68 \times 10^{13}$ W/cm^2 and 3.01×10^{13} W/cm^2. It was observed that focal plane of the beam coincided with coordinate *z*=0 for $I_0 \leq 2.68 \times 10^{13}$ W/cm^2. A shift of the focal plane toward the direction of the laser was observed for higher intensities, which can be explained by action of focusing Kerr nonlinearity. Based on that experimental evidence we have concluded that nonlinear effects (Kerr and plasma nonlinearities) were negligible for $I_0 \leq 2.68 \times 10^{13}$ W/cm^2.

Electron number generated by fs-laser laser pulse was measured using the RMS system shown in Figure 2.1. Figure 2.5(a) presents typical temporal evolution of number of electrons and amplitude of scattered microwave signal for two values of intensity $I_0 = 2.68 \times 10^{13}$ W/cm^2 and 2.93×10^{13} W/cm^2. Right and left vertical axes indicate signal directly measured by the RMS and total number of electrons in the plasma volume N_e determined using approach described in Section 2.1. The plasma decayed faster for larger laser intensities, namely two-fold decay occurs at characteristic times of 2.5 ns and 2 ns for $I_0 = 2.68 \times 10^{13}$ W/cm^2 and 2.93×10^{13} W/cm^2 respectively.

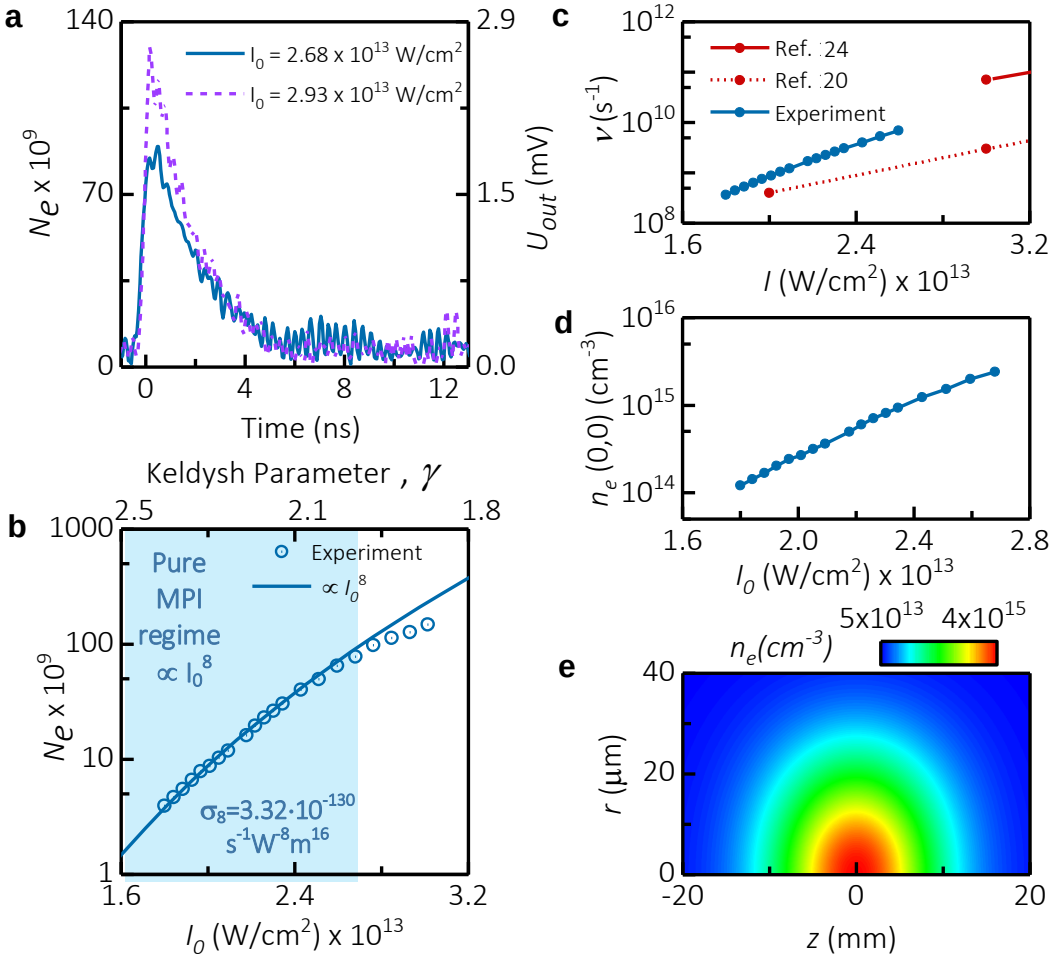

Figure 2.5. Absolute measurements of parameters of MPI in air. (a) Temporal evolution of microwave signal scattered from the plasma $U_{out}(t)$ and total number of electrons in plasma volume $N_e(t)$. (b) Measured dependence of N_e immediately after the plasma creation vs. intensity at the beam center I_0. (c) Comparison of theoretical and semi-empirical literature data with directly measured photoionization rate in this paper. Blue shaded area identifies range of intensities where pure MPI was observed $N_e \propto I_0^8$. (d) Plasma density at the beam center $n_e(0,0)$ immediately after the laser pulse vs. intensity I_0. (e) 2D distribution of plasma density immediately after the laser pulse for $I_0 = 2.68 \times 10^{13}\ W/cm^2$.

Two distinct physical processes occurring on significantly different time scales can be traced on the Figure 2.5(a). The first process is the fast rise at the moment of plasma creation (around

t=0) associated with the laser pulse passing the waist region and reaching the peak value of $N_e(t)$. The characteristic time of plasma creation is approximately the time required for light to pass the Raleigh length around the beam waist, namely $\frac{z_R}{c} \sim 0.1$ ns. The second process is the decay of the plasma remaining after the laser pulse which occurs on characteristics times of about several nanoseconds according to the Figure 2.5 (a) (see Section 2.4). RMS diagnostic was unable to temporally resolve the precise details of plasma creation due comparable response time of the system used (about 0.25 ns). However, RMS system precisely measured N_e peak value and following plasma decay $N_e(t)$ since plasma recombination is occurring on significantly slower time scale, namely several nanoseconds and, therefore, difference between the true peak value and the measured value is negligible. Note, the maximum electron number occurring immediately after the plasma creation is denoted as N_e throughout the manuscript, while the plasma decay with time is written as $N_e(t)$. Figure 2.5 (b) presents experimentally measured dependence of N_e immediately after the plasma creation vs. intensity at the beam center I_0. This peak value N_e is used to determine MPI cross-section σ_8.

Now we will determine MPI cross-section σ_8 by fitting the measured dependence of N_e vs. I_0 shown in Figure 2.5(b) using analytical expression Eq. 2.4. which shows that $N_e \propto {I_0}^8$. RMS data shown Figure 2.5(b) indicates that $N_e \propto {I_0}^8$ was satisfied with high accuracy at low intensities I_0 <2.7·10^{13} W/cm^2 which represents a clear manifestation of the pure MPI regime. Deviation from the ${I_0}^8$-law for higher intensities indicates departure from the pure MPI process at these higher I_0, which can be explained by relative proximity of Keldysh parameter γ to 1 [top horizontal axis of the Figure 2.5(b)] and action of Kerr nonlinearity. Therefore, N_e was fitted by the ${I_0}^8$-law for intensities I_0<2.7·10^{13} W/cm^2 and MPI cross-section σ_8 was determined based on the fit of this initial segment of the dependence as shown by the blue line in Figure 2.5(b) using parameters of

the laser system measured above and density of molecular oxygen in the background air $n_0 \approx 5.13 \cdot 10^{18}$ cm^{-3}. Finally, MPI cross-section was determined to be $\sigma_8 = (3.32 \pm 0.30) \times 10^{-130}$ W^{-8}m^{16}s^{-1}.

2.4 Photoionization rate and plasma dynamics

Next, we consider oxygen photoionization rates based on the measured data and compare them with data available in the literature. For laser beam center intensities $I_0 < 2.7 \cdot 10^{13}$ W/cm^2 (pure MPI regime), the dependence of photoionization rate can be readily plotted as $\nu = \sigma_8 I^8$ shown by the solid blue curve in Figure 2.5(c) using the value of σ_8 obtained above. Comparison with previously available data determined based on theoretical and semi-empirical approaches is also shown Figure 2.5(c).[22,28] The semi-empirical predictions given in Ref. [22] underestimated the photoionization rates about 2-3 times, while purely theoretical predictions in Ref. [28] seems to slightly overestimate the rates.

Experiments conducted here lay the foundations to determine plasma density distribution created in the fs-laser induced plasmas. The plasma density follows a Gaussian Distribution immediately after the laser pulse for the laser the Gaussian distribution used in this work can be written using Eq. 2.1 as: $n_e(r,z) = \sigma_8 n_0 \int I(r,z,t)^8 dt = n_e(0,0) \frac{w_0^2}{w(z)^2} e^{-\frac{2r^2}{w(z)^2}}$. Integrating the left and right side of this expression relates the plasma density at the origin location immediately after the laser pulse $n_e(0,0)$ with the directly measured quantities of N_e, w_0 and z_R by $n_e(0,0) = \frac{N_e}{\frac{231\pi}{1024 \cdot 16} \pi w_0^2 z_R}$. Figure 2.5(d) shows the dependence of $n_e(0,0)$ on laser intensity. Figure 2.5 (e) shows the 2D distribution of plasma density $n_e(r,z)$ for $I_0 = 2.68 \times 10^{13}$ W/cm^2.

Dr. M. N. Shneider has numerically simulated the plasma decay to validate our experimental measurements as shown in Figure 2.6. Plasma decay was simulated using a 1D axially symmetric model in radial direction which self-consistently integrates the Navier-Stokes, electron heat conduction, and electron-vibration energy transfer equations.[70] The model accounts for recombination of molecular ions, attachment processes, formation and decay of complex ions, electron energy losses due to electronic, vibrational excitations and elastic scattering.

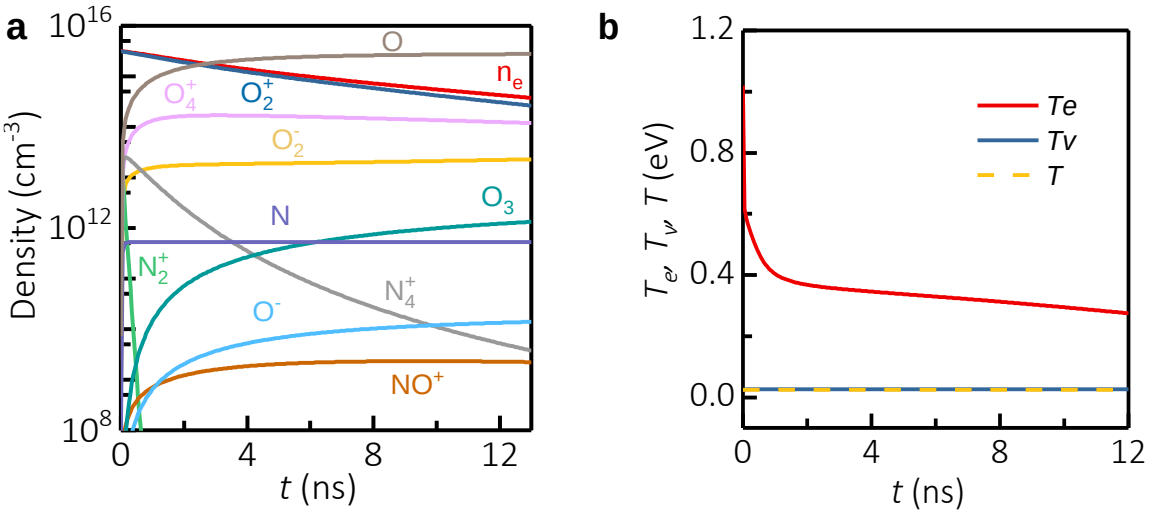

Figure 2.6. Numerical simulations of plasma decay. Plasma decay of after fs-laser pulse for $I_0 = 2.7 \cdot 10^{13}\ W/cm^2$. (a) Plasma species (b) Electron, vibrational and gas temperatures.

Simulated decay of the densities and temperatures of various plasma species at the point of origin are shown in Figure 2.6 for intensity in the beam center, $I_0 = 2.7 \times 10^{13}\ \mathrm{W/cm^2}$. Extremely fast (< 1ns) decrease of electron temperature to about 0.4 eV is associated with electron energy loss due to vibrational excitation of molecules, while slower later decay is governed by elastic collisions. Plasma density in the center decayed twice in about 3.2 ns, which is primarily dominated by dissociative and three-body recombination of molecular ions. Slightly faster plasma

decay times observed in the experiments (about 2.5 ns) might be related to presence of water vapor in the ambient air.

In summary, we have presented methodology which is paving the way for precise determination of the physical constants of multi-photon ionization, namely cross-section and photoionization rate. The method utilizes precise measurement of the spatial and temporal distributions of the laser beam intensity and absolute measurement of total electron number in the plasma volume by means of elastic scattering of microwaves off the plasma volume and absolute calibration of the microwave system using dielectric scatterers. We have demonstrated capability of this method on the example of eight-photon ionization of molecular oxygen and determined the corresponding MPI cross-section to be $\sigma_8=(3.32\pm0.30)\cdot10^{-130}$ $W^{-8}m^{16}s^{-1}$.

The results presented in this chapter were published in Refs. 1.1, 2.1 and 2.2 listed in the PUBLICATIONS section.

3. FS-LASER-INDUCED MULTIPHOTON IONIZATION IN VARIOUS GASES AT 1 ATM

Modified from Paper published in *J. Appl. Phys.* **125**, 193301 (2019).

Animesh Sharma, Mikhail N. Slipchenko, K. Arafat Rahman, Mikhail. N. Shneider & Alexey Shashurin

3.1 Experimental Details

Schematic of the experimental setup is shown in Figure 3.1.

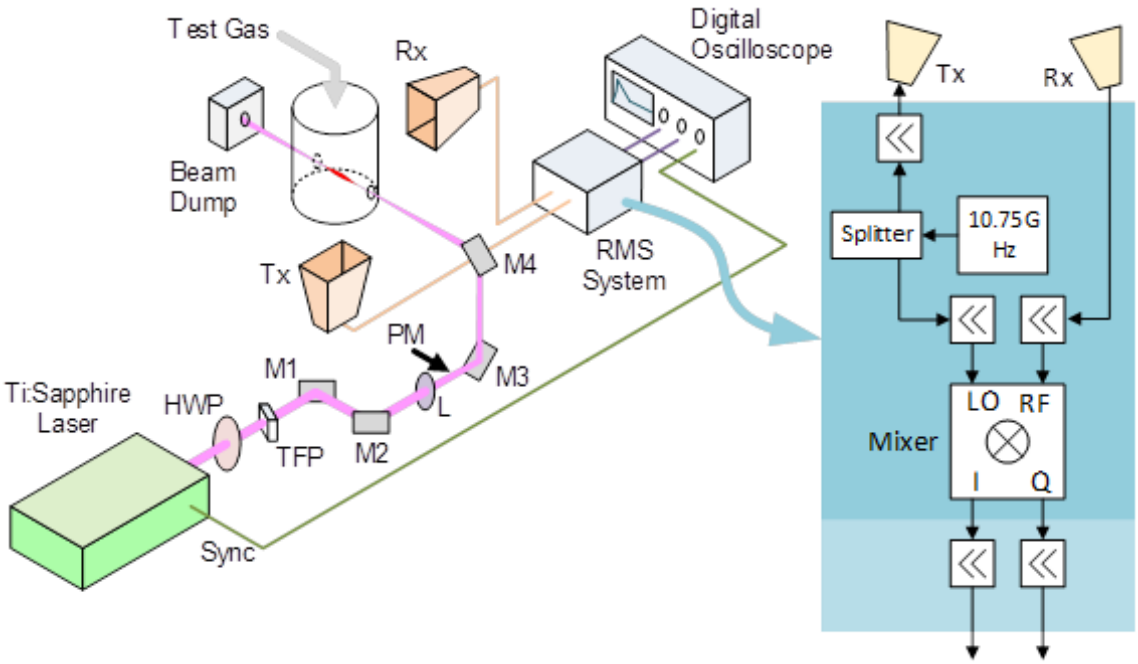

Figure 3.1. Femtosecond laser experimental setup and RMS homodyne measurement system. Laser operates at 800 nm wavelength with 100 Hz repetition rate. HWP: half wave plate, TFP: thin film polarizer, PM: power meter, L: 1 m plano-convex lens. The RMS system based on homodyne architecture. For the dielectric scatterers, the output signal is recorded right after the mixer without additional amplification (32 dB power). Test gases: *O_2, Xe, Ar, N_2, Kr,* and *CO*.

A regeneratively amplified Ti:Sapphire laser system (Solstice Ace; Spectra Physics, Inc.) was used as the fs-laser source having 126 fs Gaussian temporal width at 800 nm wavelength, which was focused into a positive pressure chamber using a plano-convex spherical lens of 1 m focal length. The laser was operated at 100 Hz repetition rate. The diameter of the beam incident on the lens was 7 mm. A half wave plate and thin film polarizer were used to control the irradiance of the beam, which was measured using a laser power meter (Gentec-EO XLP12-3S-H2-DO) placed after the lens. The positive pressure chamber was made in-house. Thin polyethene film was used for the walls of the chamber. It had small apertures for entry and exit of the laser beam and to maintain a continuous flow of the gas. The duration of the pulse was measured using single shot autocorrelation (TiPA, Light Conversion, Inc.) and was logged throughout the experiment to ensure no drift in laser characteristics was taking place. For this work the measured beam waist and Rayleigh length were w_o=93.6 μm, z_R=26.9 mm, respectively.

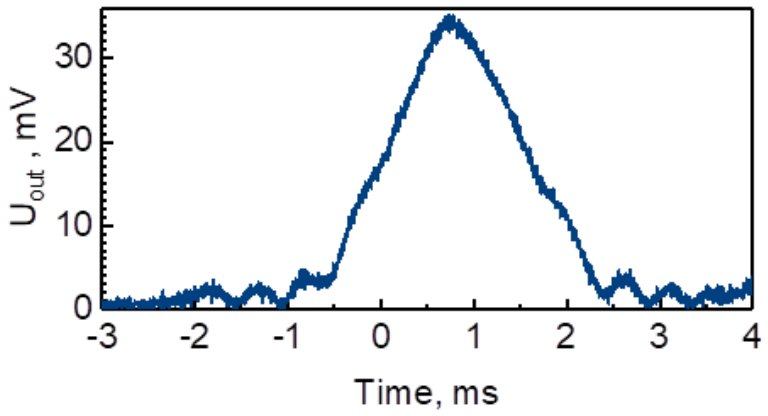

Figure 3.2. Response of the RMS system obtained from dielectric scatterer. Temporal evolution of microwave signal scattered due to Teflon bullet was used for calibration of the RMS system.

For this experiment, a homodyne detection-based RMS system operating at frequency 10.75 GHz was used to irradiate the plasma volume. The calibration of the RMS system was done by using Teflon dielectric bullets having a cylindrical shape with length 10 mm, diameter 3.175 mm

and relative permittivity 2.10. The bullet was propelled using a pneumatic gun through the microwave field. The path of dielectric scatterer was chosen to be same as the path of the laser beam in the later experiments. Figure 3.2 shows the output signal of the RMS system produced by Teflon bullet. The system calibration coefficient was found to be $A = 6.72 \times 10^5\ \mathrm{V\Omega m^{-2}}$.

Experimental setup shown in Figure 3.3 was used to study the contribution of the non-linear processes in the laser beam propagation.[72] The system used the same 1000 mm lens as used in the setup shown in Figure 3.1. The diverging beam after the focus was reflected from a pair of beam sampler onto a beam profiler. Each reflection reduced the intensity of the beam by 95%. $D4\sigma$ beam diameter was measured by Newport LBP2-VIS2 Laser Beam Profiler. Measurements of the beam diameter were made for different pulse energies at two locations after the focus. The details of the measurements and analysis of the results are presented below.

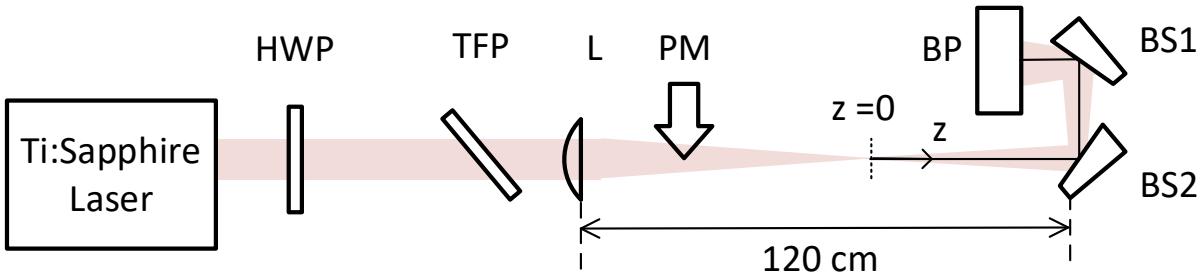

Figure 3.3. Experimental system used to study contribution of the non-linear processes in the laser beam propagation. Beam profile was measured using laser beam profiler (BP) located at distance z=67 cm for different beam irradiances. A pair of wedge beam samplers (BS) was used to reduce the irradiance of the beam after focus to prevent saturation of BP.

Photograph of the microwave system used in this experiment is shown in Figure 3.4.

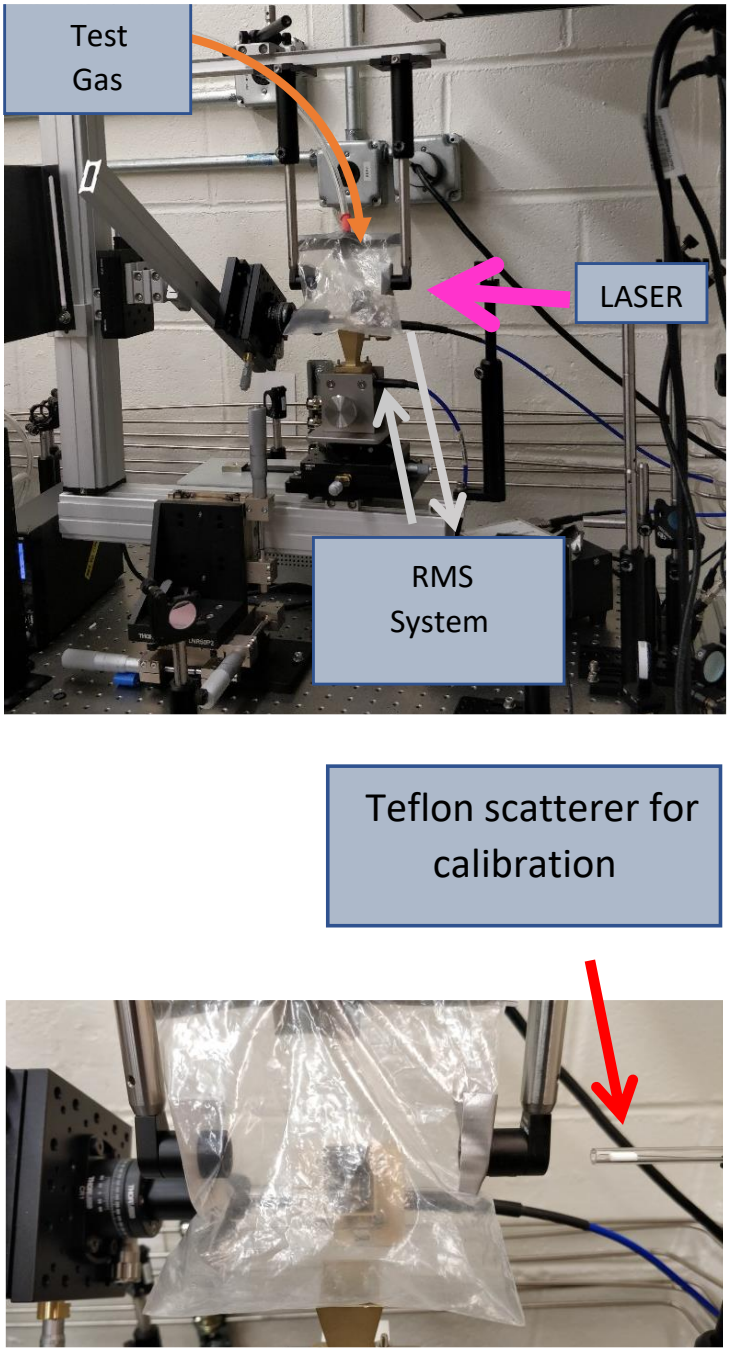

Figure 3.4. Photograph of the RMS system used in the experiment

3.2 Nonlinear optical effects

The moment of inception of non-linear effects was determined using the setup shown in Figure 3.3. To this end, the beam radius w was measured in ambient air at a location after the focus, namely z=67 cm for different laser pulse energies. Figure 3.5 shows the dependence of beam radius vs. laser pulse energy and demonstrates three characteristic images of the beam profiles taken for E_0=80, 280 and 640 μJ. One can see that beam radius has saturated at 2.1mm with 5 % accuracy for $E_0 < 280\ \mu$J. However, there is rapid decrease in size for $E_0 > 280$μJ. The change in beam size can be seen in Figure 3.5 (b). The image is nearly identical for E_0=80μJ and 280 μJ but for E_0=640 μJ, the beam has reduced in size. The beam waist diameter was calculated using D4σ method. The reduction in the beam size is attributed to non-linear Kerr effect near the focal region (Kerr effect dominates over the plasma non-linearity at low end of laser irradiances).[21,72] Thus, it can be concluded that threshold of non-linear effect inception in air corresponds to the laser pulse energy of E_0=280 μJ and corresponding irradiance, I_0=6.47·10^{12} W/cm^2.

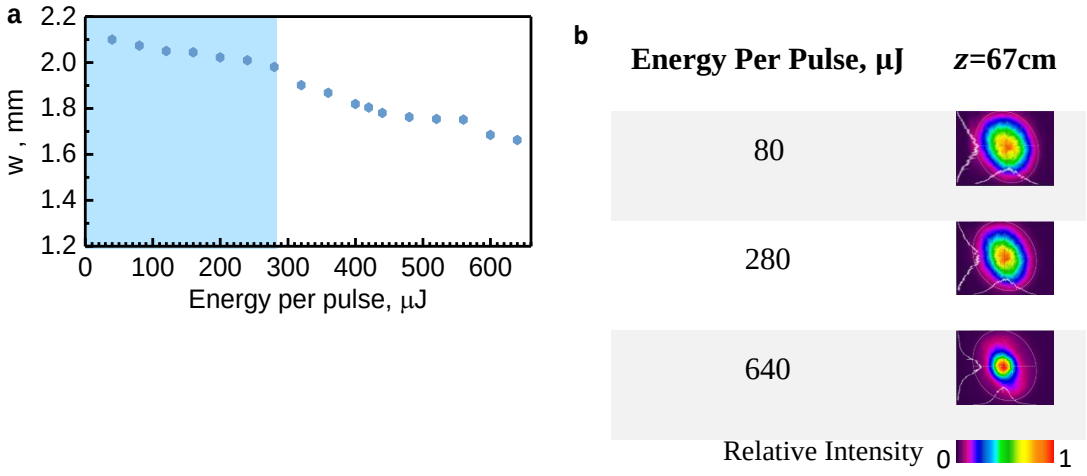

Figure 3.5. Measurements of inception of non-linear optical effects in air. (a) Dependence of the laser beam radius $w = \sqrt{(D4\sigma_x \cdot D4\sigma_y)/4}$ at a location after the focus (z=67 cm) vs. laser pulse energy E_0. (b) Images of the laser beam profiles for E_0=80, 280 and 640 μJ.

3.3 Photoionization rates

Based on the findings in Section 3.2, low laser pulse energies in the range of 220-300 μJ were used for determination of photoionization rate and electron number density in O_2 as detailed below. The non-linear effects are negligible in that range of energies and, therefore, the Gaussian beam distribution in vicinity of the focal plane can be used $I(r,z,t) = I_o\left(\frac{w_o}{w(z)}\right)^2 exp\left(-\frac{2r^2}{w(z)^2}\right) exp\left(\left(\frac{t-t^*}{\tau}\right)^2\right)$, $w(z) = w_0\sqrt{1+\left(\frac{z}{z_R}\right)^2}$, where τ is the characteristic temporal width of the beam ($\tau = \sqrt{2}\tau_{\mathrm{Gauss}}$), w_0 is the radius of beam waist and z_R is the Rayleigh length , r is the radial distance from the beam axis, z is the axial location and t is the time, I_0 is the beam irradiance at center ($r = 0, z = 0$). Cross-section of eight-photon ionization of oxygen molecule σ_8 was determined directly from the measurements of spatial and temporal characteristics of the laser beam (τ, w_o and z_R), measurements of N_e by RMS system for different laser intensities, and using expression $N_e = \frac{231\pi}{1024\cdot 16}\sqrt{\frac{\pi}{8}}\sigma_8 n_0 \tau\pi w_0^2 z_R \cdot {I_0}^8$ following the methodology described in detail in Section 2.1. It was observed that proportionality law $N_e \propto {I_0}^8$ was satisfied with high accuracy in experiments. Multiphoton ionization rate of O_2 at atmospheric pressure (defined as $\nu = \sigma_8 I^8$) and plasma density in the centre of the plasma spark ($n_{e0} = \frac{N_e}{\frac{231\pi}{1024\cdot 16}\pi w_0^2 z_R}$) are plotted in

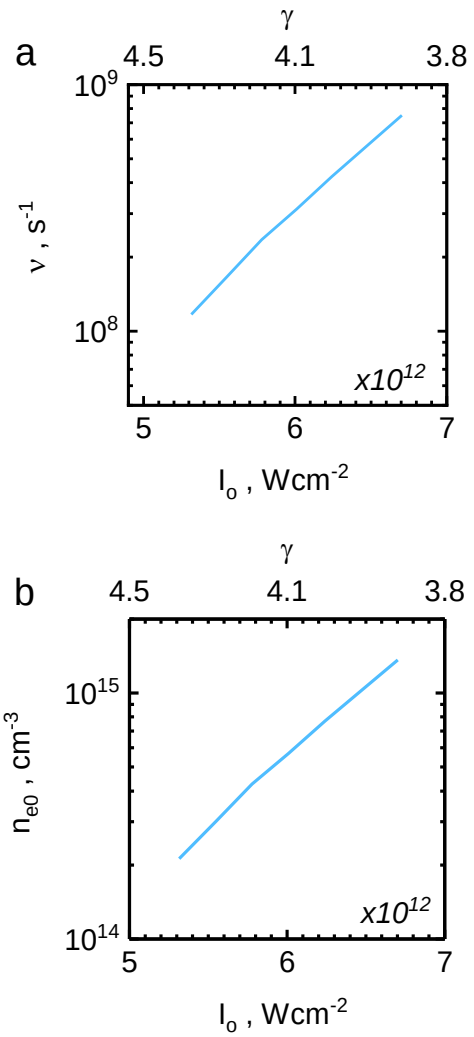

Figure 3.6. Multiphoton ionization of oxygen by femtosecond laser pulse (wavelength 800 nm) vs. irradiance at the waist I_o. The Keldysh parameter is shown on the top horizontal axis. (a) Multiphoton ionization rate, (b) Plasma density vs. irradiance at the center.

Figure 3.7 presents log-log plot of the total number of electrons in the plasma after laser pulse as a function of laser pulse energy in *Xe*, O_2, *Kr*, *CO*, N_2, and *Ar*. These experiments were conducted at atmospheric pressure and intensities when Gaussian beam intensity distribution does not apply due to non-linear phenomena. Therefore, in these experiments, only temporal dynamics of total number of electrons $N_e(t)$ was determined without making any additional assumptions on the intensity distribution in the laser beam.

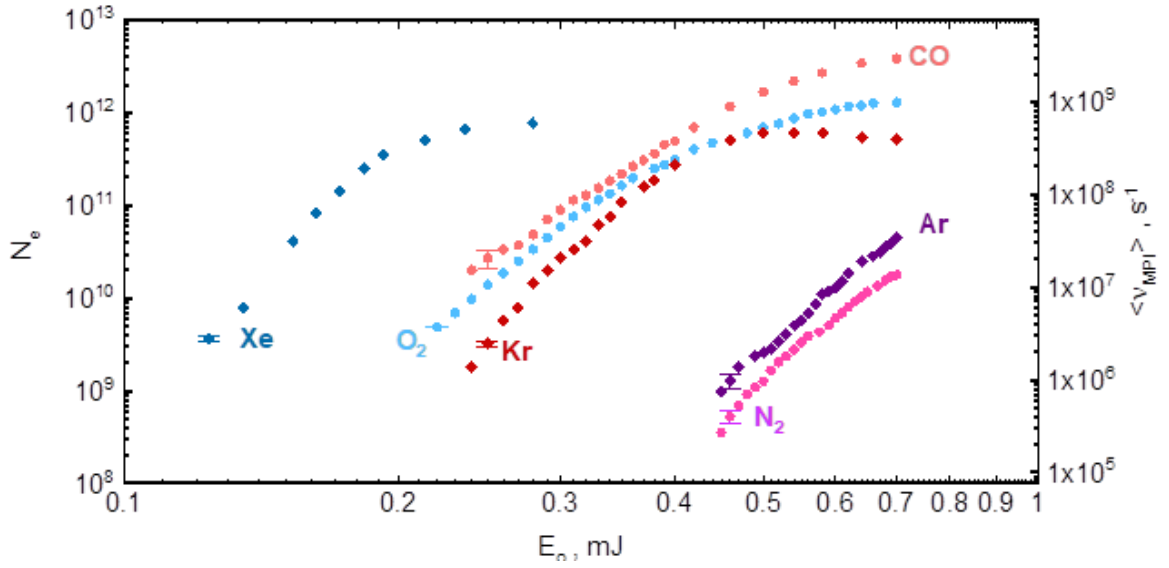

Figure 3.7. Total number of electrons generated by photoionization of different gases by laser pulse having Gaussian duration 126 fs and 7 mm diameter focused using 1,000 mm lens

One can observe the following features in Figure 3.7. Firstly, the energy requirement for electron generation in various gases increases going from left to right in Figure 3.7 and the total number of electrons produced by the laser pulse in all gases increases as a power function of pulse energy. Deviation in power law is seen at higher energies in *Xe*, O_2, *Kr* and *CO*. *Xe* is ionized the most to produce the highest number of electrons from the same pulse energy compared to other gases in the experiment whereas N_2 produces the least. Secondly, the ionization of *Xe* is ~2 orders of magnitude greater than O_2 for 220 μJ after which electrons generation in *Xe* significantly flattens. Electron numbers generated in *Ar* ($\mathcal{E}_i$ =15.7 eV) is 1.5 times greater that N_2 ($\mathcal{E}_i$ =15.6 eV) for the energy range 450-700 μJ, where $\mathcal{E}_i$ is the first ionization potential. Ionization in *CO* is 10 times greater than *Kr* at lower pulse energies (240 μJ) and the difference decreases to 2.5 times (370 μJ). Further increasing the pulse energies results in increasing difference in the electron production. Thirdly, at higher pulse energies the electron production starts to saturate. The

saturation sets in at 180 μJ in *Xe*, 370 μJ in *Kr*, 320 μJ in O_2 and 400 μJ in *CO*. In N_2 and *Ar*, there is no onset of saturation for the pulse energies used in the experiments. The saturation in electron production seen in *Xe*, O_2, *Kr* and *CO* is attributed to the defocusing of the laser by the plasma filament itself.[72,28,70,22] Increasing the pulse energy, increases the electrons number and consequently, the electron density in the plasma filament. The plasma defocusing reduces the laser intensity and limits the ionization.

3.4 Plasma decay

Temporal decay of electrons is presented in **Error! Reference source not found.**. Electron decay in *Ar*, *Kr*, *Xe*, and N_2 can be explained by analysis of two competing processes, namely, creation of new electrons by ionization of the metastable atoms M^* (where $M = Ar, Kr, Xe$, or N_2) at collision with electrons and loss of the electrons due to almost instant conversion of M^+ to M_2^+ and following dissociative recombination.

$$\frac{\partial n_e}{\partial t} = k n_e n_{M^*} - \beta n_e^2 \qquad \text{Eq. 3.1}$$

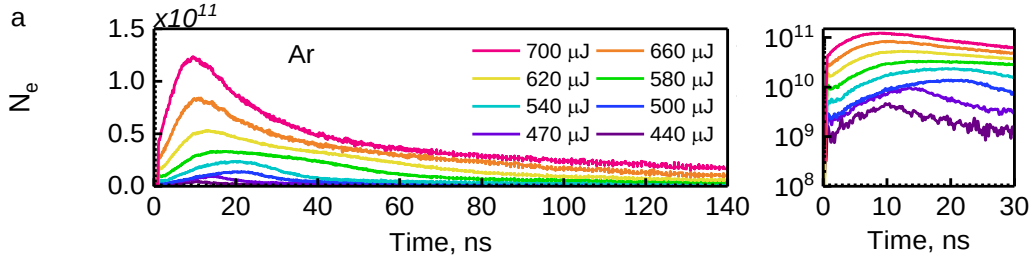

Figure 3.8. Temporal evolution of electron numbers in different gases (a) Ar, (b) Kr, (c) Xe, (d) N_2 (e) O_2, (f) CO

Figure 3.8. Continued

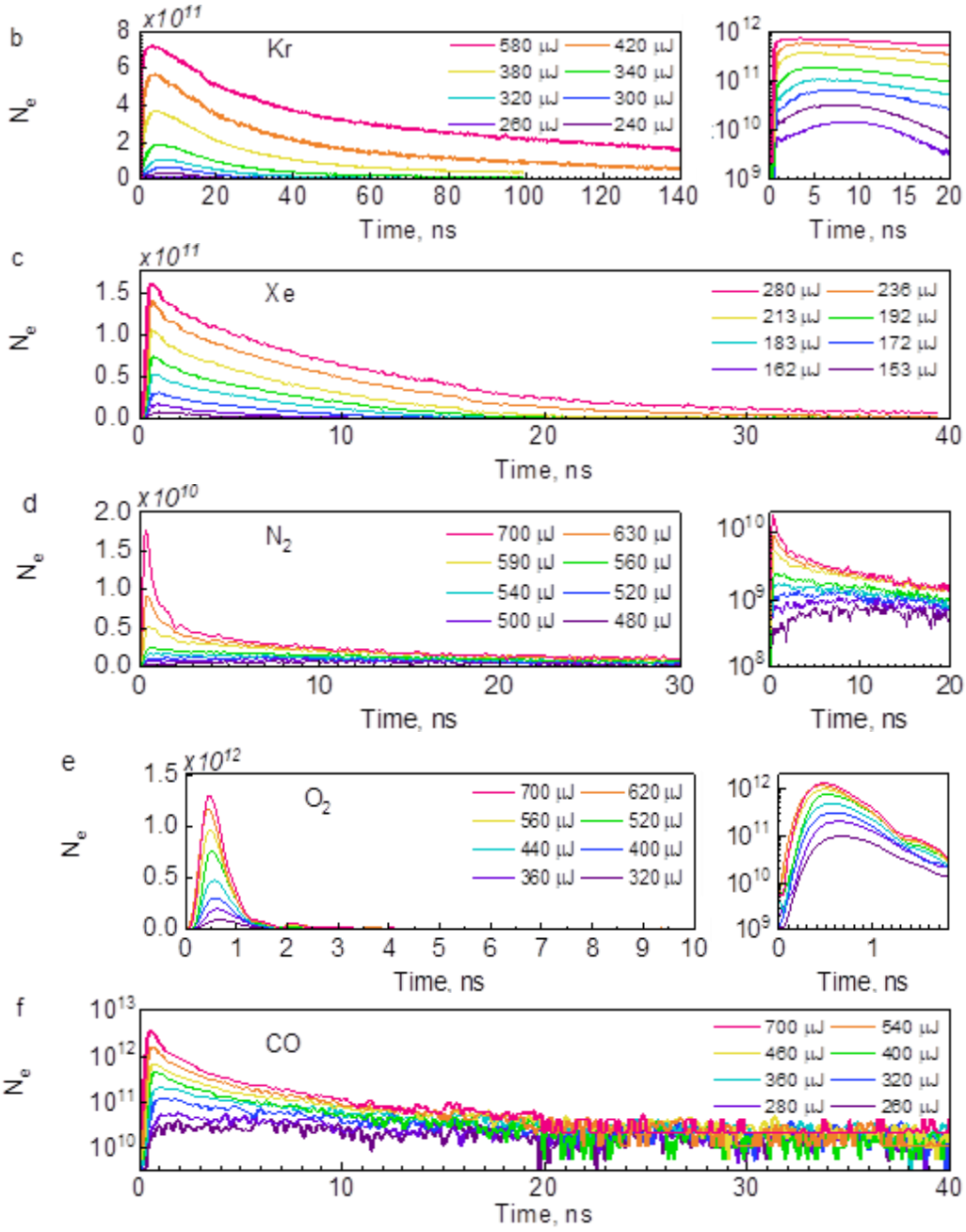

In *Xe* and *N2* the recombination term remains dominant throughout the plasma decay $\beta n_e > k n_{M^*}$, so that number of plasma electrons always decreased with time. Anomalous temporal evolution of N_e was observed in *Ar* and *Kr*; namely, one can see that N_e continues to increase even after the laser pulse. This behavior can be potentially explained by high metastable density n_{M^*}

and thus dominant role of the ionization term immediately after the laser pulse $\beta n_e > k n_{M^*}$. Thus, $\frac{\partial n_e}{\partial t}$>0 immediately after the laser pulse and number of plasma electrons increased correspondingly. On later stage of the decay, number of metastable atoms decreased and recombination term started to dominate, causing further reduction of N_e with time. Time corresponding to the peak value of N_e can be used to estimate the plasma density in the laser-induced plasma. Indeed, $t_{peak} = 1/\beta n_e$, so using $\beta \approx 10^{-7}$ cm^3/s [65] and experimentally observed t_{peak}~10 ns, the plasma density can be estimated as $n_e \sim 10^{15}$ cm^{-3}.

O_2 and *CO* are characterized by high electron affinity, so additional electron loss mechanism, electron attachment, must be added to the right-hand side of the Eq. 3.1: $-\nu_a n_e$. In these gases, electron attachment mechanism dominates the overall electron loss and causes significantly faster N_e decay observed on the time scale ~ 1 ns in the experiments shown in **Error! Reference source not found.**(e) and **Error! Reference source not found.**(f). These decay times can be supported by the theoretical estimations. The rate of three-body attachment electron to oxygen molecule can be calculated using $\nu_a = k_{O_2} \cdot n_{O_2}^2$. The reaction constant k_{O_2}=2.5·10^{-30} cm^6/s [65,56] gives the electron attachment rate $\nu_a \approx 10^9$ s^{-1} and corresponding electron decay time $\tau_a = \frac{1}{\nu_a} \approx 1$ ns.

In summary, we have measured the total number of electrons created by intense near-infrared femtosecond laser pulse in *O_2, Xe, Ar, N_2, Kr* and *CO* at atmospheric pressure. The method is based on elastic scattering of microwaves off the plasma volume and absolute calibration of the microwave system using dielectric scatterers with known properties. Point of inception of non-linear optical effects in air was determined and photoionization rate in oxygen was determined for lower laser intensities (< 6.47·10^{12} W/cm^2). Electron decay after the laser pulse was consistent with competition of two processes, namely, creation of new electrons by ionization of the

metastable atoms at collisions with electrons and electron loss due to dissociative recombination and attachment to oxygen. The tabulated data of experimentally measured electron numbers generated in a laser induced spark provides accurate way for validation of physical models and provides input for simulation of these processes.

The results presented in this chapter were published in Refs. 1.3 and 2.3 listed in the PUBLICATIONS section.

4. REMPI-RMS DIAGNOSTICS OF *CO* AT ELEVATED PRESSURES

Modified from article *accepted with minor revisions*

Animesh Sharma, Erik L. Braun, Adam R. Patel, Mikhail N. Slipchenko , K. Arafat Rahman, Mikhail N. Shneider , and Alexey Shashurin

4.1 Four energy level model of *CO* molecule

We will consider a four (4) energy level model of *CO* molecule being irradiated by 230.1 photons in a fs-laser pulse.[45] Simultaneous absorption of two photons excites the molecules from the ground state 1 to the state 3 ($B^1\Sigma^+$), and an additional photon absorption causes ionization (state 4). The system of equations governing the population densities in each level is given below.

$$\begin{aligned}
\frac{dn_1}{dt} &= -W_{13}n_1 + (Q_{21} + A_{21})n_2 + (W_{31} + Q_{31} + A_{31})n_3 \\
\frac{dn_2}{dt} &= -(Q_{21} + A_{21})n_2 + (Q_{32} + A_{32})n_3 \\
\frac{dn_3}{dt} &= W_{13}n_1 - (W_{31} + Q_{31} + A_{31} + Q_{32} + A_{32} + P_{ion})n_3 \\
\frac{dn_4}{dt} &= P_{ion}n_3
\end{aligned} \qquad \text{Eq. 4.1}$$

where n_i - the number density of *CO* molecules in i^{th} level, W_{13}- rate of the two-photon absorption (from level 1 to 3), Q_{ij} - quenching rates from i^{th} to j^{th} level, A_{ij} - rates for spontaneous emission and P_{ion}- ionization rate from level 3. The two-photon absorption rate W_{13} and the ionization rate P_{ion} can be expanded as follows:

$$W_{13} = \sigma_2 I^2$$

$$P_{ion} = \sigma_{ion} I$$

Eq. 4.2

where σ_2 is the cross section for the TPA process and σ_{ion} is the cross-section for the ionization process

The evolution of number density of *CO* molecules in the resonant state n_3 and electron number density (equal to that of *CO* ions $n_e = n_+ = n_4$) will be now considered in more details since these parameters govern signals directly measured by the LIF and MS diagnostics. Specifically, the rate equations for the corresponding quantities can be re-written by combining the various Q_{ij} and A_{ij} together to the form:[73]

$$\frac{dn_3}{dt} = W_{13} n_1 - (W_{13} + A + Q + P_{ion}) n_3$$

$$\frac{dn_e}{dt} = P_{ion} n_3$$

Eq. 4.3

System of equations (4) can be further simplified based on order of magnitude analysis of the rates reported in literature and eliminating the negligible terms. Analysis of the available data indicates that, for the case of fs-laser (pulse duration τ=126 fs~10^{-13} s), terms $W_{13}n_3$, $An_3$and Qn_3 can be neglected compared to the $\frac{dn_3}{dt} \sim \frac{n_3}{\tau}$ since $W_{13}\tau \ll 1$, $A\tau \ll 1$ $Q\tau \ll 1$, while term $P_{ion}\tau$ can be potentially significant. Indeed, the two-photon absorption rate W_{13} can be expanded as a product of cross-section and laser irradiances, and for laser pulse having a wide linewidth (~200 cm^{-1}) significantly larger compared to the width of the transition (~0.2 cm^{-1}) it can be estimated as

$W_{13} \sim 10^7$ s^{-1}.[74,75] The quenching rate is proportional to the pressure ($Q/p = 8$ MHz/Torr), so that $Q \sim 10^9 - 10^{10}$ s^{-1}.[76] The spontaneous emission is typically determined from the radiative decay time ($A = 1/\tau_A \sim 10^8$ s^{-1}).[77] Limited data on the ionization cross-section values can be found in Ref. [78]. Finally, the system of equations 4.3 can be reduced to the form:

$$\frac{dn_3}{dt} = W_{13} n_1 - P_{ion} n_3$$

$$\frac{dn_e}{dt} = P_{ion} n_3 \qquad \text{Eq. 4.4}$$

Signals measured by the LIF and MS diagnostics are governed by the system of equations 4.4. The solutions of 4.4 can be analyzed in two operation regimes:

- ***Excitation-dominated case*** ($P_{ion}\,\tau \ll 1$). In this case, majority of the *CO* molecules participated in the TPA are in the excited state 3 by the end of the laser pulse, while fraction of those being ionized is low. These conditions are satisfied when the photoionization rate P_{ion} is low, so that term $P_{ion} n_3 \ll \frac{dn_3}{dt}$ and can be neglected. The number of excited *CO* molecules n_3 is increasing linearly with time throughout the entire laser pulse duration and does not reach steady-state. The solutions of (5) for number densities n_3 and n_e and corresponding scaling laws can be written as:

$$n_3 = W_{13} \tau n_{CO} \propto I^2 n_{CO}$$

$$n_e = P_{ion} \tau n_3 \propto I^3 n_{CO} \qquad \text{Eq. 4.5}$$

$$n_{CO} \gg n_3 \gg n_e$$

where I is laser intensity. Finally, local relations for the number densities n_3 and n_e can be expanded into the approximate scaling laws for actual quantities measured by LIF and MS techniques assuming that laser beam absorption and nonlinear optical effects are small along the entire propagation path:

$$S_{LIF} \propto E^2 n_{CO}/Q \propto E^2 n_{CO}/p$$

$$N_e \propto E^3 n_{CO} \qquad \text{Eq. 4.6}$$

- ***Ionization dominated case*** ($P_{ion}\tau \gg 1$). In this case, majority of the *CO* molecules participated in the TPA are ionized by the end of the laser pulse, while fraction of those being in excited state 3 is low. These conditions are satisfied when the photoionization rate is high so that n_3 does saturate at $t \sim \frac{1}{P_{ion}}$ after the laser pulse initiation at value: $n_3 = \frac{W_{13}}{P_{ion}} n_1$. Electron number density can be expressed as $n_e = P_{ion}\tau\, n_3 = W_{13}\tau\, n_1$. The number densities n_3 and n_e and corresponding scaling laws can be written as:

$$n_3 = \frac{W_{13}}{P_{ion}} n_{CO} \propto I n_{CO}$$

$$n_e = W_{13}\tau\, n_{CO} \propto I^2 n_{CO} \qquad \text{Eq. 4.7}$$

$$n_{CO} \gg n_e \gg n_3$$

Similarly, the scaling laws for the actual quantities measured by LIF and MS techniques can be written as:

$$S_{LIF} \propto En_{CO}/Q \propto En_{CO}/p$$

$$N_e \propto E^2 n_{CO}$$

Eq. 4.8

One can see from this analysis, that photoionization deexcitation pathway cannot overpower the fluorescence in case of pressure increase. Indeed, the probabilities of the *CO* molecule to be ionized/excited are determined by the laser intensity only and independent of the pressure. Therefore, increase of pressure (at constant mole fraction) causes proportional increase of number density of excited *CO* molecules n_3 contributing to the fluorescence. Finally, the LIF signal regardless of particular regime (excitation- of ionization-dominated) remains constant with the pressure increase since increase of number of $n_3 \propto n_{CO}$ is exactly compensated by the proportional increase of p.

4.2 Experimental Details

In this study, a cavity dumped, q-switched regeneratively amplified Ti-sapphire laser having 800 nm wavelength, ~100 fs full width half-maximum temporal width, operating at 1 kHz pule repetition rate was used as a source. The beam from the source was sent to an optical parametric amplifier and after several mixing processes the desired wavelength of 230.1nm was obtained, the detail of which are presented in Ref. [17]. The beam was focused using 150 mm cylindrical lens into high pressure test cell as shown schematically in Figure 4.1. The test cell had optical access provided by four UV fused silica windows, 38.1 mm in diameter and 12.7 mm in thickness. Some experiments at atmospheric pressure were conducted in an in-house made positive pressure chamber fabricated from thin polythene sheets and equipped with apertures for entry and exit of the laser beam as shown schematically in Figure 4.2.

The number of electrons generated from REMPI were measured using a single horn microwave scattering systems implemented using a homodyne architecture. Microwaves from source at 10.75 GHz were split in two arms. One arm was connected to a circulator output of which was amplified and transmitted via WR 75 standard gain horn antenna with a 10dB nominal gain. The horn was oriented such that the electric field was along the longer dimension of the plasma. The scattering signal was collected by the same horn and was amplified before being connected to RF port of *I/Q* mixer. The second arm from the splitter was amplified and connected to LO port of the *I/Q* mixer. The two outputs of the *I/Q* mixer were further amplified and connected to a digital oscilloscope for acquisitions.

Experiments were conducted in CO/N_2 mixtures at pressures 1, 3 and 5 bar and *CO* fractions of 4%, 6%, 20% and 100% as detailed

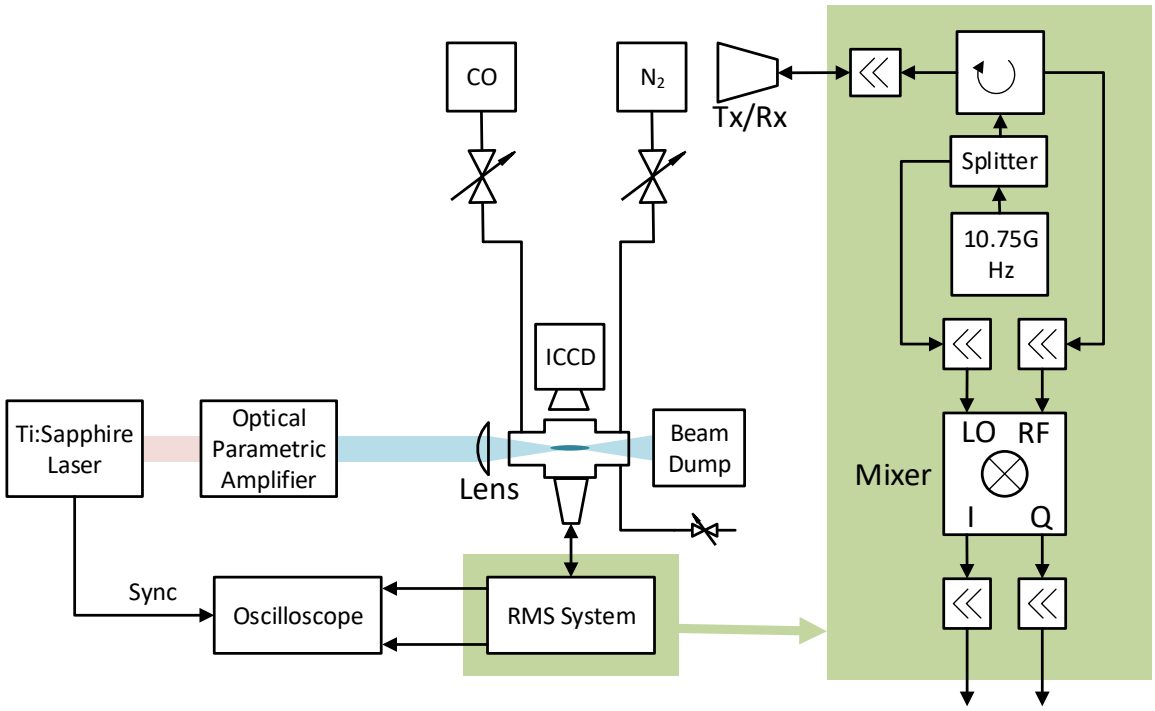

Figure 4.1. Schematic of the experimental REMPI arrangement with RMS measurement system in test cell.

The optical components such as the windows and lens were individually calibrated. The transmission coefficient for each was calculated as the ratio of energy entering the component and leaving the component. The transmission coefficient for the entry window (85.85%), exit window (86.72%) and the focusing lens (70.87%) were found the be invariant in the wavelength and energies used for this study. The experiment to determine the energy absorbed at the beam propagation through the test cell were conducted by measuring the power before the focusing lens and leaving the chamber after the exit window. The transmission coefficients were then used to determine laser energy inside the chamber right after the entry window and before the exit window.

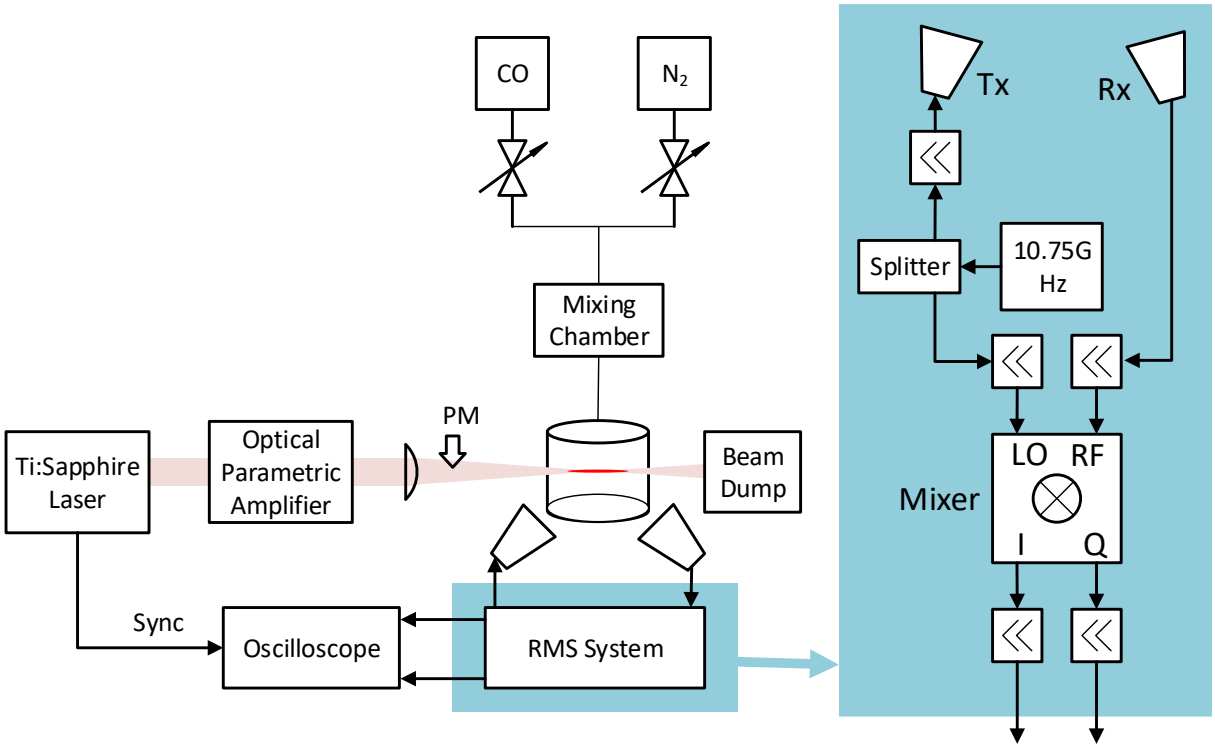

Figure 4.2. Schematic of the experimental REMPI arrangement with RMS measurement system in positive pressure chamber.

Photographs of the laser system and test cell used in experiments are shown in Figure 4.3 and Figure 4.4, respectively.

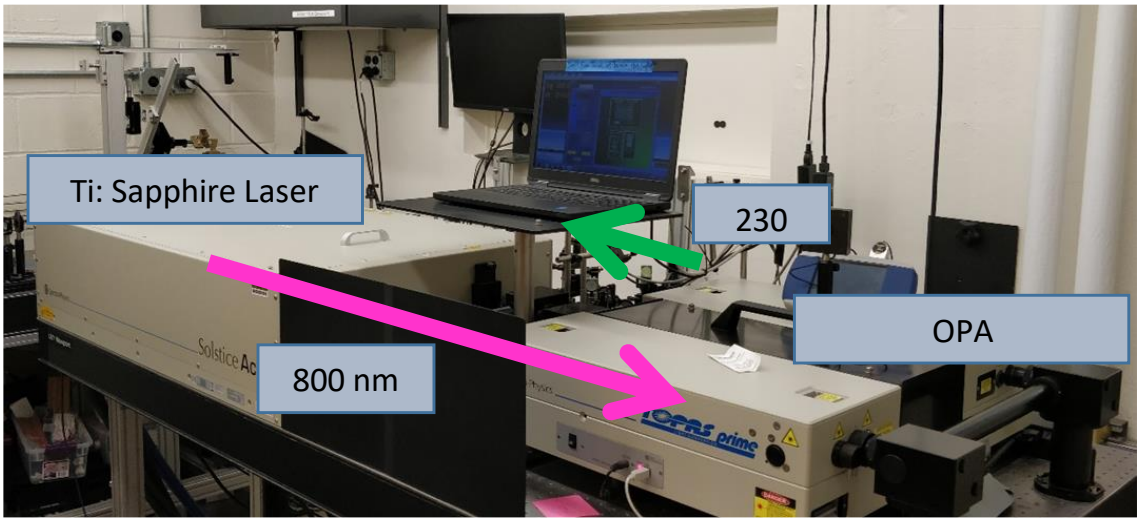

Figure 4.3. Photograph of the laser system used in experiments.

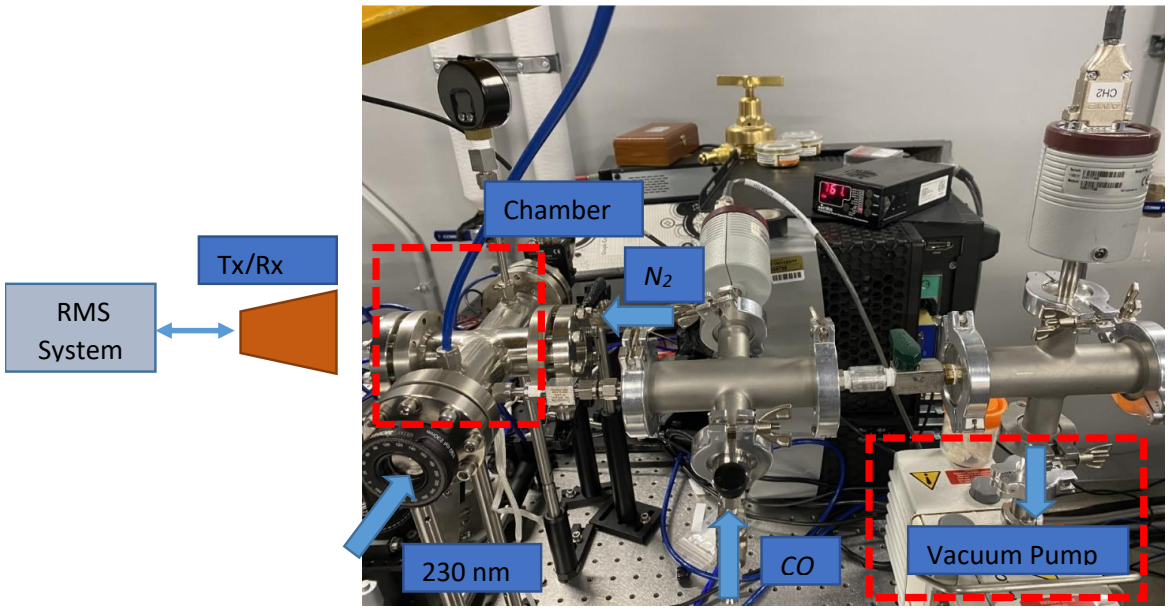

Figure 4.4. Photograph of the test cell along with the pumping system used in experiments.

4.3 Experimental demonstration of REMPI-RMS method

The exact wavelength corresponding to the 2+1 REMPI of *CO* was determined by means of spectral scanning of the laser and simultaneous monitoring of the REMPI-induced electron numbers by the RMS technique. The typical temporal evolution of the RMS signal and number of electrons generated by 12 μJ laser pulse in 5 bar of 20% *CO* is presented in Figure 4.5(a), and the maximal value at $t \approx 0$ is proportional to the number of electrons produced by the laser pulse since collisional processes and avalanche ionization are disabled for the short fs-laser pulse used in this work. Figure 4.5(b) presents the number of the laser-generated electrons as function of the laser wavelength expressed in relative units, and one can see that it peaked at 230.1 nm corresponding to 2+1 REMPI of *CO*. The FWHM of the resonant curve was ~ 1.2 nm. The laser was tuned exactly to 230.1 nm in the subsequent experiments.

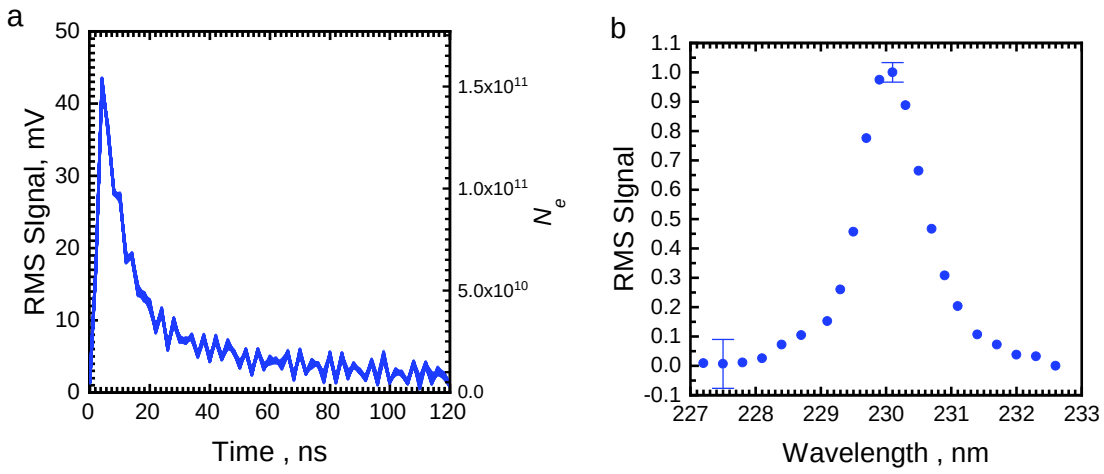

Figure 4.5 (a) Temporal evolution of RMS signal and electron number produced by the laser pulse at 230.1 nm (5 bar, 20% *CO*, 12 μJ) , (b) Number of the REMPI-generated electrons as function of the laser wavelength expressed in relative units.

The number of REMPI-generated electrons at 230.1 nm (N_e) in CO/N_2 mixtures at pressures 1, 3 and 5 bar and selective *CO* fractions of 4%, 6%, 20% and 100% are shown in Figure 4.6. One can see that N_e increased with the laser pulse energy E_0 which can be explained by the higher laser intensity in the focal region and, therefore, higher photoionization rates. The average plasma volume was estimated $3 \cdot 10^{-3}$ cm^3 based on ICCD photography and, therefore, average electron number density was in the range 10^{13}-10^{14} cm^{-3} for the experimental conditions used in this work.

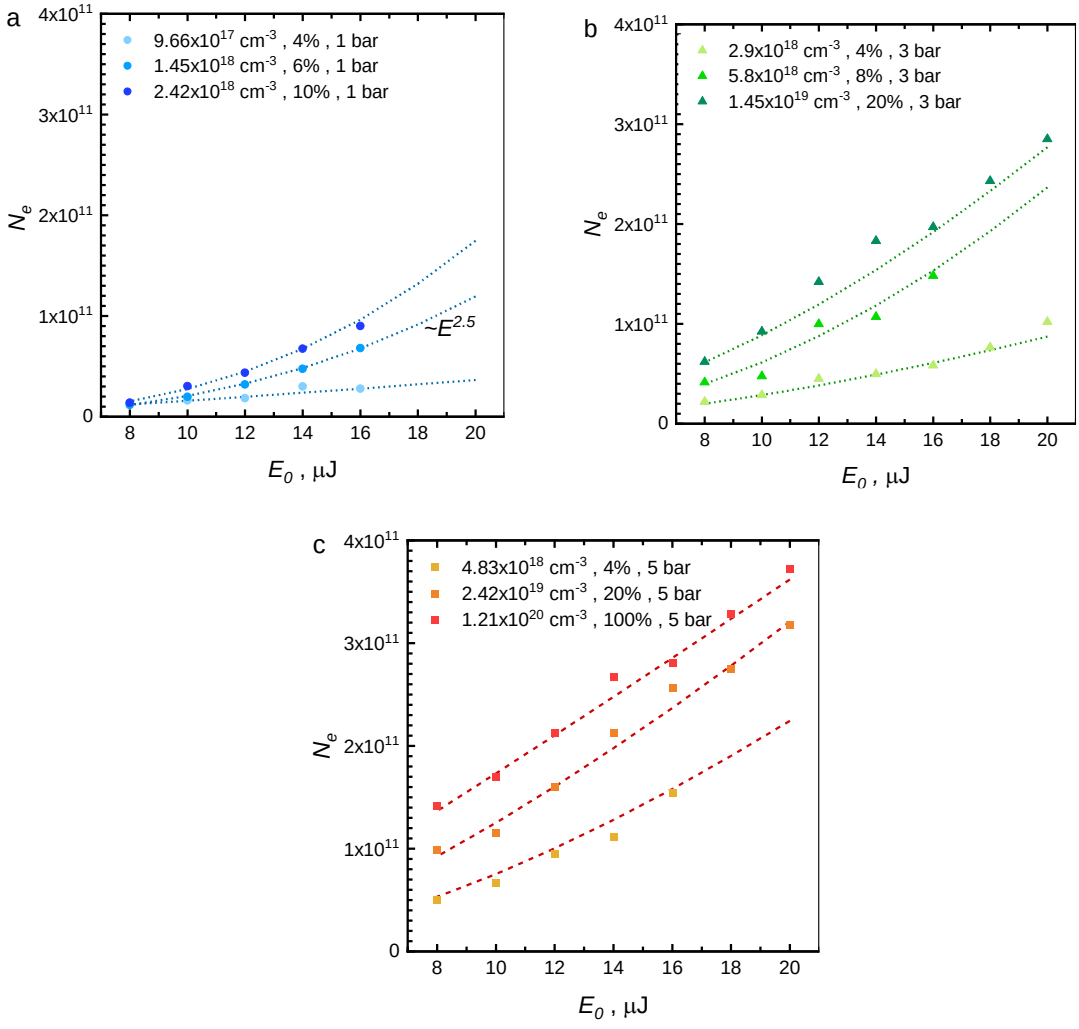

Figure 4.6. The number of REMPI-generated electrons (N_e) in CO/N_2 mixtures at pressures 1, 3, and 5 bar and selective *CO* fractions of 4%, 6%, 10%, 20%, and 100% as function of laser pulse energy E_0. (a) 1 bar, (b) 3 bars, (c) 5 bars.

One practical way to analyze the data presented above is to plot N_e vs. *CO* number density (n_{CO}) for the different laser pulse energies as shown in Figure 4.7. One can see that the data points for the different pressures collapsed to a single curve which is fully-governed by the n_{CO} value. This fact indicates that number of REMPI-generated electrons is governed by n_{CO} only and independent of the amount of the buffer gas (for the tested pressure range p=1-5 bars). This effect can be associated to the selectivity of the REMPI process which mainly ionizes *CO* molecules and leaves the buffer gas particles unaffected.

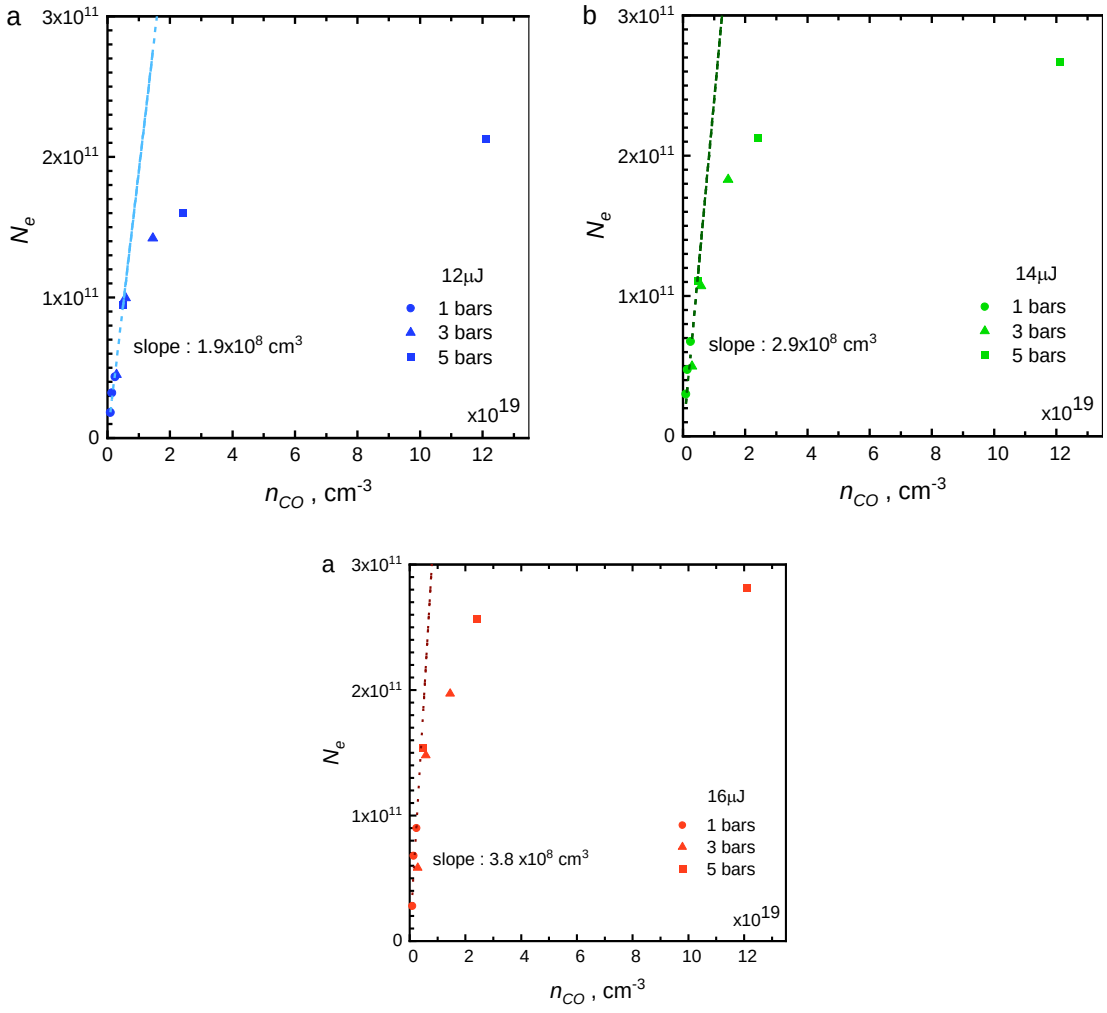

Figure 4.7. The number of REMPI-generated electrons (N_e) in *CO*/N_2 mixtures as function *CO* number density (n_{CO}) for different laser pulse energies. (a) 12 μJ, (b) 14 μJ, (c) 16 μJ.

Additionally, Figure 4.7 indicates that number of REMPI-generated electrons increased proportionally with n_{CO} up to about $n_{CO}\approx5\cdot10^{18}$ cm^{-3} and then started to saturate. This behavior can be attributed to reduction of the laser beam energy reaching the focal zone as n_{CO} increases due to the two-photon absorption occurring along the path of the laser beam propagation. This effect will be analyzed and quantified in details below in the next section.

The effect reported in Figure 4.7 that the number of REMPI-generated electrons is fully-governed by the n_{CO} and independent of the amount of the buffer gas for the range of pressures p=1-5 bar has practical importance and can be used for diagnostic purposes. Indeed, linear portion of the curves presented in the Figure 4.7 (for $n_{CO}\leq5\cdot10^{18}$ cm^{-3}) can be used as a calibration plot for the measurements of n_{CO} in *CO*-containing mixtures at pressures up to 5 bar. Specifically, the number of REMPI-generated electrons N_e should be first measured in the mixture under test by means of the RMS technique for a given laser pulse energy E_0, and then corresponding n_{CO} should be determined from the calibration curve. The laser pulse energy can be chosen based on the specific requirements to the sensitivity and dynamic range of the n_{CO} measurement. Specifically, larger laser pulse energies are associated with higher sensitivity while smaller maximal measurable n_{CO} value.

4.4 Discussion of scaling laws: 2+1 REMPI and fluorescence

We will now analyze and discuss the experimentally observed trends of N_e vs. laser pulse energy and N_e vs. n_{CO} presented in Figure 4.6 and Figure 4.7 in conjunction with four (4) energy level model of *CO* molecule presented in Section 4.1.

The number of the REMPI-generated electrons followed nearly $N_e \propto E^{\sim(2.5-3)}$ according to the data presented in Figure 4.6. This allows to conclude the excitation-dominated regime in vicinity of the beam focal plane then the excitation dominates over the ionization ($n_3 > n_{co}^+ = n_e$), and the following scaling laws for number of REMPI-generated electron and LIF signal: $N_e \propto E^3 n_{CO}$ and $S_{LIF} \propto E^2 n_{CO}/Q \propto E^2 n_{CO}/p$ as detailed in Section 4.1.

We will now focus on scaling of N_e with n_{CO} presented in Figure 4.7. Firstly, initial linear portion of the dependence and its slope are consistent with $N_e \propto E^3 n_{CO}$ scaling law in excitation-dominated regime. Indeed, one can see that 30 % increase of the laser pulse energy from 12 to 16 μJ led to about two-fold increase in the slope from $1.9 \cdot 10^{-8}$ to $3.8 \cdot 10^{-8}$cm^3 which agrees with the scaling law.

Secondly, to explain the saturation onset of the N_e vs. n_{CO} dependence experimentally demonstrated in Figure 4.7 for n_{CO} >$5 \cdot 10^{18}$ cm^{-3}, the measurements of the laser pulse energy absorbed in the TPA process during the passage through the *CO*/N_2 gaseous mixture (ΔE_{TPA}) were conducted. ΔE_{TPA} was determined by subtracting the actual energy entering the gas volume E from that exiting the gas volume measured using the methodology described in Section 4.2. The results of these measurements are shown in Figure 4.8. Specifically, Figure 4.8(a) shows fraction of the energy loss $\Delta E_{TPA}/E$ expressed in percent vs. n_{CO} for various laser pulse energies, and one can see that $\Delta E_{TPA}/E$ increased with n_{CO} and reached about 10-15% at n_{CO} = (5-7)$\cdot 10^{18}$ cm^{-3} for the tested range of laser pulse energies. Due to fast cubic increase of N_e with laser energy $N_e \propto E^3 n_{CO}$ in the excitation-dominated regime, one should expect deviation from the initial linear scaling of N_e with n_{CO} even at relatively small laser absorption levels. Indeed, if simple criteria for the saturation onset of 30-50% drop of the initial linear scaling factor is chosen, one should expect the onset when just 10-20% of the laser pulse energy is absorbed. The laser absorption data presented

in Figure 4.8(a) indicates then that the saturation onset should be expected at n_{CO} = (5-7)·10^{18} cm^{-3}, which agrees well with the experimental findings in Figure 4.7.

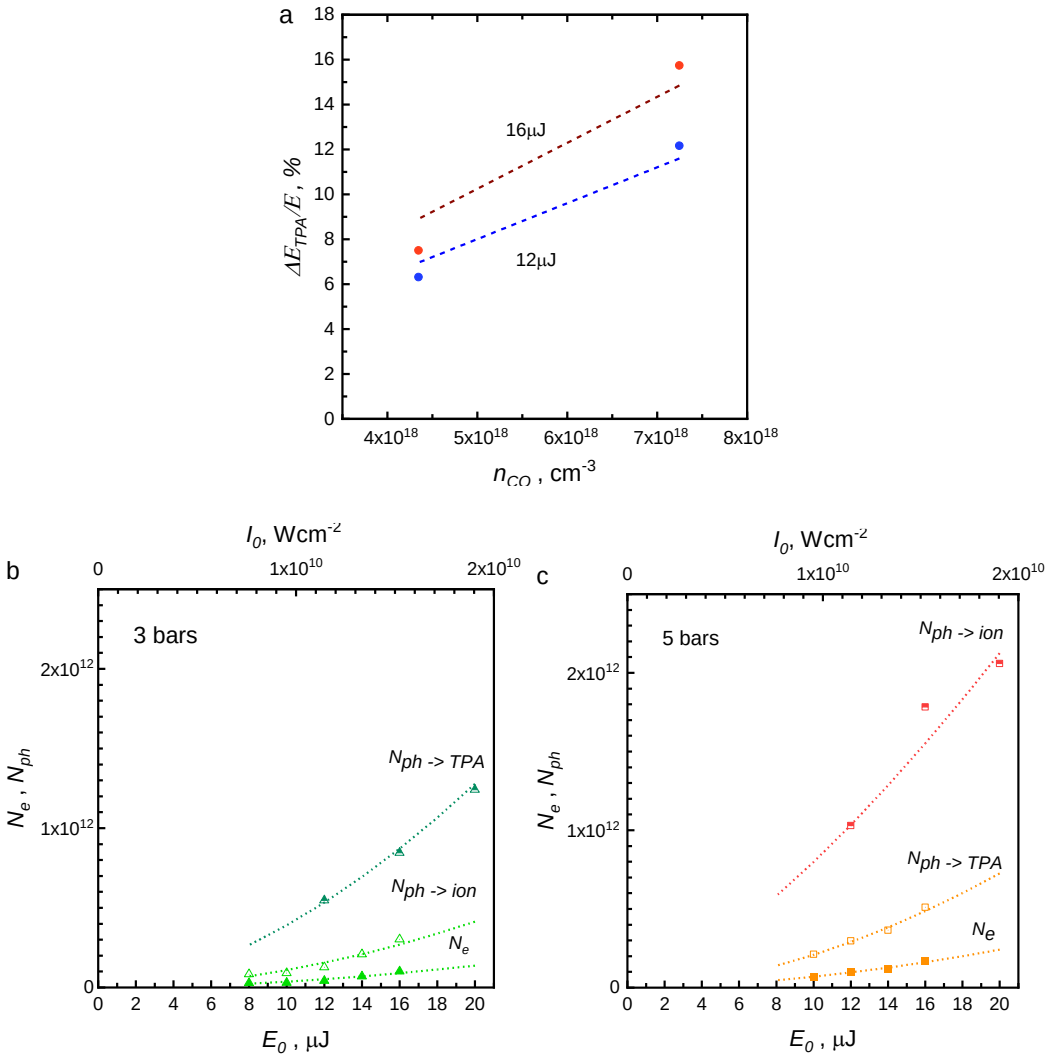

Figure 4.8. Laser energy loss data due to the TPA process in CO/N_2 mixture. (a) Fraction of the energy loss $\Delta E_{TPA}/E$ expressed in percent vs. n_{CO} for various laser pulse energies. (b) and (c) Number of REMPI-generated electrons (N_e), number of photons consumed for ionization $N_{ph\to ion} = 3N_e$, and number of photons absorbed in the TPA process in CO/N_2 mixture $N_{ph\to TPA}$ as function of laser pulse energy E_0 for 3 and 5 bars.

The laser pulse absorption measurements allow also to directly quantify fractions of excited (N_3) and ionized ($N_+ = N_e$) *CO* molecules after the laser pulse passage. Figure 4.8(b) and Figure 4.8 (c) shows ΔE_{TPA} and corresponding number of photons absorbed in the TPA process as the laser beam passes through the test cell determined as $N_{ph\to TPA} = \frac{\Delta E_{TPA}}{h\nu}$, where ν – laser frequency and h- Planck constant. These absorbed photons can contribute to production of either ionized and excited *CO* molecules in the mixture right at the end of the laser pulse since other transitions are disabled on the time scale of the short fs-laser pulse as discussed in Section 4.1. Specifically, each ionization consumes three photons, while each excitation act consumes two photons, so it can be written: $N_{ph\to TPA} = N_{ph\to ion} + N_{ph\to exc} = 3N_+ + 2N_3$. Figure 4.8 shows the number of photons required to create N_e electrons which was plotted as $N_{ph\to ion} = 3N_e$ based on the RMS data. One can see that total number of photons $N_{ph\to TPA}$ was about 3-fold larger than $N_{ph\to ion}$: $N_{ph\to TPA} \approx 3N_{ph\to ion}$, and thus, number of the excited molecules was about 3-fold lager than number of the ionized molecules $N_3 \approx 3N_+$.

4.5 Applicability limits of REMPI-RMS technique

In general, measurements by the proposed REMPI-RMS technique are practically feasible only within the region of linear scaling of N_e with n_{CO} (see Figure 4.7). From one hand, this requires to stay prior to the saturation onset of the dependence shown in Figure 4.7. The saturation onset corresponds to substantial laser energy absorption while it passes through the gaseous mixture, and, therefore, one requirement for the applicability of REMPI-RMS technique is to satisfy of the low-absorption criteria $\Delta E_{TPA}/E << 1$. From the other hand, sufficiently large slope of the dependence N_e vs. n_{CO} is needed to enable measurements of low n_{CO} values.

High end of the measurable n_{CO}-range is associated with use of laser intensity sufficiently low to satisfy the low-absorption criteria $\Delta E_{TPA}/E$<<1, while remaining within the sensitivity limit of the RMS system. Indeed, highest n_{CO} value measurable with the system developed in this work was n_{CO}=5·10^{18} cm^{-3}. To enable the measurement of 10-fold larger n_{CO}, it would require to reduce laser energy 10 times to keep satisfying the low-absorption criteria since $\Delta E_{TPA}/E \propto E n_{CO}$. This in turn would reduce number of electrons and RMS signal about 100 times since $N_e \propto E^3 n_{CO}$. We estimate that upper limit of n_{CO}=10^{20} cm^{-3} is feasible for the REMPI-RMS technique but future experiments are required to confirm this.

Low end of the measurable n_{CO}-range is associated with use of high laser intensities limited by the nonlinear optical phenomena. In this work we utilized moderate laser intensities (~10^{10} W/cm^2 as shown in Figure 4.8) in the focal region followed these used in recent TP-LIF experiments in Ref [48]. In principle, these intensities can be substantially increased (2 orders of magnitude) by utilization of the spherical lens rather than cylindrical and increase of the laser pulse energy (see Sections 2 and 2.4). The 100-fold increase of the laser intensity in the focal region would allows 10^6 times reduction of the n_{CO} value while keeping same electron number density ~10^{14} cm^{-3} due to the scaling law $n_e \propto I^3 {n_{CO}}^3$. The electron number density of the order 10^{14} cm^{-3} was achieved in this work using cylindrical lens, while this is still within the sensitivity limits of the RMS system even if spherical lens is used based on the data reported in Sections 2 and 2.4. Finally, we estimate that low limit of n_{CO} ~10^{11} cm^3 is feasible by means of increase of laser intensity to ~10^{12} W/cm^2 in the focal region. Low-absorption requirement $\Delta E_{TPA}/E$<<1 will be automatically satisfied in this case. Also, it is worth noting that ionization-dominated regime can be approached at these high intensities ($P_{ion}\tau \geq 1$).

These preliminary considerations show that n_{CO} can be measured in a large range of n_{CO}=10^{11}-10^{20} cm^{-3} by means REMPI-RMS technique if laser intensity in the focal region is properly tuned. Further experiments are needed to determine this range precisely. In addition, particular choice of the laser pulse spatial and temporal properties, and optical components utilized in the system can be tailored for each the specific experiment to further expand the measurable range of n_{CO}.

4.6 Spatially-resolved measurements with REMPI-RMS technique

Preliminary experiments demonstrating feasibility of spatially-resolved measurements by REMPI-RMS technique were conducted in atmospheric air using MPI induced by 800 nm photons. The Ti:Sapphire laser operating at 800 nm having Gaussian temporal width of 126 fs at 1 kHz repetition frequency. The beam was focused and reflected using a series of planoconvex lens and plane mirrors to create plasma at three locations separated by 1.5 cm. The beam is first passed first through a 500 mm lens then through a 250 mm lens and finally a 300 mm lens. Standard homodyne-based two-horn RMS system at 10.75 GHz described in more details in Section 3.1 was utilized in these experiments.

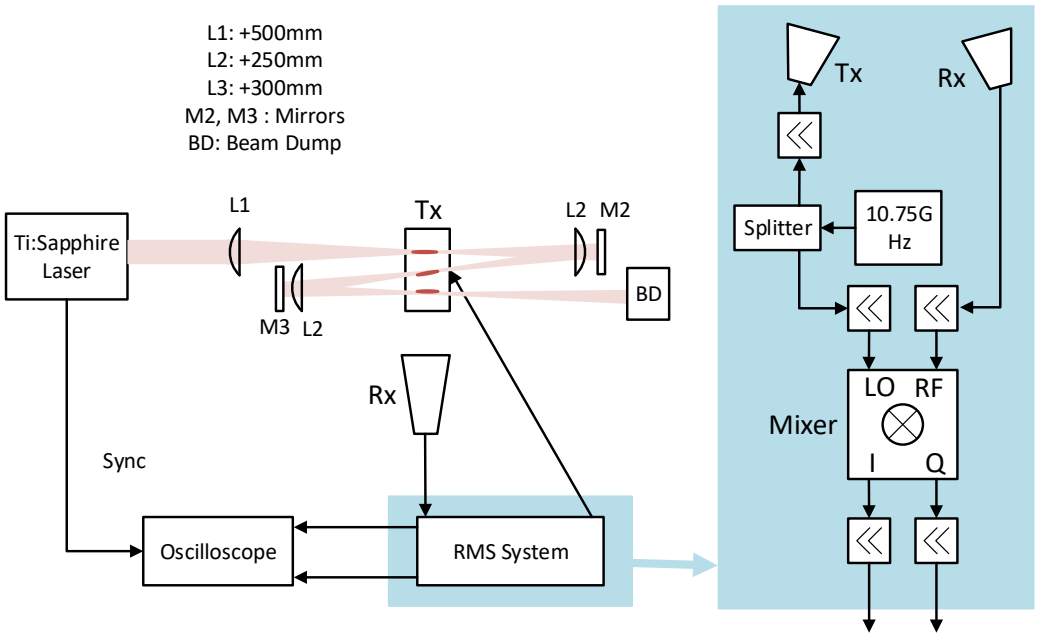

Figure 4.9. Experimental setup for creating and detecting multiple induced sparks

The photograph of system in operation is shown in Figure 4.10. One can see series of three sparks induced by the single laser pulse.

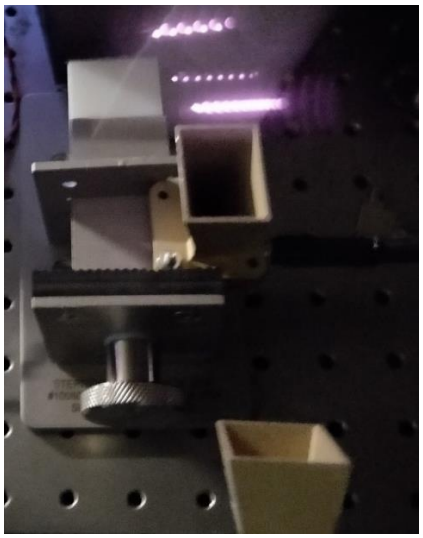

Figure 4.10. Series of three sparks created in air using single 800 nm fs-laser pulse separated about 1.5 cm apart

Figure 4.11 presents the output signal measured by the RMS system. The three peaks correspond to the three laser-induced sparks produced as result of the consecutive reflections of the laser pulse by the mirrors. The peaks have two characteristic time scales. Each peak has a fast rise time of ~0.5 ns indicating moment of plasma creation by the laser pulse and subsequent plasma decay on the scale ~1 ns. The temporal separation between the peaks corresponds to the time for light to travel from one focal location to the other. Specifically, peak P1 corresponds to the laser focusing produced by 500 mm lens, P2 is due to 250 mm lens and P3 is due to 300 mm lens.

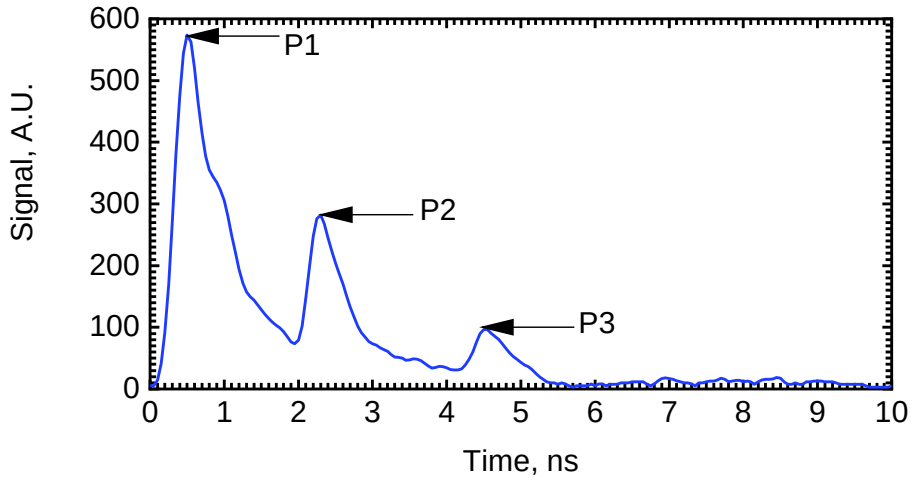

Figure 4.11. Output of RMS system from detection of three consecutive laser sparks. P1, P2 and P3 are produced by 500mm, 250mm and 300mm plano-convex lens respectively.

There are several reasons affecting amplitude each individual peak. First, each spark is positioned uniquely with respect to the radiation/detecting horn of the RMS system. Therefore, the strength of the detected signal varies depending on the distance from the spark to the horn. Individual location of each spark defines a unique calibration constant to be used for transformation from the RMS signal to absolute number of electrons. Second, large probing volume increases the RMS signal since it is proportional to the plasma volume. Specifically, the P1 500 mm lens has the larger probe volume in comparison with P2 250 mm lens and P3 300 mm

lens. Third, there is a finite loss of the laser pulse energy in the mirrors since the mirrors are not fully reflective.

Therefore, the idea of the spatially-resolved measurements are as follows. Single laser pulse can be used to create series of laser sparks at different spatial locations. The calibration constant relating signal at particular spark to the absolute number of electrons can be determined for each spark in the series using standard approach of dielectric scatterers used throughout this work. Then, absolute electron number measurements can be conducted in several locations by single laser pulse. The method has potential to be extended to operate with REMPI process and with larger number of sparks for measurements of 1D or 2D distributions of number densities of species.

In conclusion, we have demonstrated the use of RMS technique to detect multiple sparks induced by a single laser pulse. These finding are paving the way for creation of REMPI-RMS diagnostic technique allowing measurements of number density of selected species (e.g. *CO*) in several spatial locations using single laser pulse.

The results presented in this chapter were published in Refs. 1.4, 2.4 and 2.5 listed in the PUBLICATIONS section.

5. CONCLUSIONS

This section deals with the conclusion drawn from the current study of photoionization in various gases and implementation of REMPI-RMS hybrid technique for diagnostics of particular component in a gaseous mixture at elevated pressure.

5.1 Summary and Conclusions

Chapter 1 provides an overview of laser induced plasmas. A brief overview of lasers was presented and the fundamental process of photoionization and its various regimes namely Tunneling Ionization (TI), Multi-Photon Ionization (MPI) and Resonance-Enhanced Multi-Photon Ionization (REMPI) were described. The theory behind Rayleigh Microwave Scattering (RMS) as a method for diagnostics of small plasma objects was discussed as well. The potential of laser-induced plasma in the domain of combustion diagnostics was introduced.

Chapters 2 and 3 dealt with study of MPI of various gases including O_2, *Xe*, *Ar*, N_2, *Kr*, *CO* and air at atmospheric pressure and room temperature by means of RMS diagnostics. A methodology for precisely determining the physical constants of multi-photon ionization, namely cross-section and ionization rate was created. The method utilizes precise measurement of the spatial and temporal distributions of the laser beam intensity and absolute measurement of total electron number in the plasma volume by means of RMS diagnostics based on elastic scattering of microwaves off the plasma volume and absolute calibration of the microwave system using dielectric scatterers with known properties.

First, the capability of this method on the example of eight-photon ionization of molecular oxygen of the ambient air was demonstrated and corresponding MPI cross-sections were

determined. Second, the methodology was applied to study MPI in various pure gases including O_2, *Xe*, *Ar*, N_2, *Kr*, and *CO* at atmospheric pressure. Point of inception of nonlinear optical effects in air was determined and the photoionization rate in oxygen was found for lower laser intensities ($<6.47 \times 10^{12}$ W/cm^2). Third, electron decay after the laser pulse was analyzed in conjunction with 1D axially symmetric model. The decay was consistent with the competition of two processes, namely, creation of new electrons by ionization of the metastable atoms at collisions with electrons and electron loss due to dissociative recombination and attachment to oxygen. The tabulated data of experimentally measured electron numbers generated in a laser-induced spark provide an accurate method for validation of physical models and an input for numerical simulation of these processes.

In chapter 4 , combination of REMPI and subsequent detection of the numbers of REMPI-generated electrons by RMS technique were used to measure *CO* number density in nitrogen buffer, and potential of the corresponding diagnostics approach for measurements of species number density in gaseous mixtures was demonstrated. Number of REMPI-induced electrons scaled linearly with *CO* number density up to about n_{CO}=5·10^{18} cm^{-3} independently of buffer gas pressure up to 5 bar. This region of linear scaling of N_e with n_{CO} can be used for diagnostics of absolute number density of *CO* in mixtures. Following increase of n_{CO} caused saturation onset due to the laser beam energy loss while laser pulse is travelling through the gaseous mixture. A four energy level model of *CO* molecule was developed and direct measurements of the laser pulse energy absorbed in the two-photon process during the passage through the *CO*/N_2 mixture were conducted to analyze the observed trends of number of REMPI-generated electrons with n_{CO} and laser energy.

5.2 Recommendations for future work

This section recommends future work based on the results obtained in this work.

Firstly, future studies should continue effort on the tabulation of the cross-sections and photoionization rates of the multi-photon ionization for more pure gases and laser wavelengths (from UV to mid-IR) using the methodology proposed and validated in this work. This effort would provide critical experimental evidence for various fields utilizing laser-induced plasmas and theoretical modeling of these.

Secondly, REMPI-RMS technique should be further investigated. Preliminary analysis conducted in this work shows that n_{CO} can be measured in a range of n_{CO}=10^{11}-10^{20} cm^{-3} if laser intensity in the focal region is properly tuned. The next step in this area would be to conduct measurements of number densities in this extensive range and obtain the experimental confirmation for the range of REMPI-RMS technique applicability. Also, studying REMPI-RMS technique with high intensities (~10^{12} W/cm^2) would be important as in this case ionization-dominated regime can be reached.

Thirdly, REMPI-RMS technique should be tested for measurements in real combustion systems. The first goal could be to conduct experiment in Hencken burner flame at atmospheric pressures and then experiments in high-pressure combustion systems should be planned.

Fourthly, utilization of microwave scattering technique can be expanded to the measurements of microplasmas at rarified gas pressures. Range of pressures below several Torr corresponds to the Thomson scattering regime, when microwave frequency is exceeding electron collisional frequency with gas participles. Then, the electrons are in free motion since no collisions occur on the period of the incident microwave field oscillation. In this case, signal measured by the microwave scattering system is independent of the electron-gas collisional frequency which

greatly simplifies the interpretation of the measurement results. The idea of current REMPI-RMS technique could be further expanded for measurements of number densities of selective species in rarified gases in Thomson regime. This can be beneficial for the area of electric propulsion diagnostics, e.g., for measurements of number density of neutral *Xe* inside the slit of Hall thrusters.

Fifthly, further study of the spatially resolved measurements utilizing multiple laser sparks should be conducted and expanded for use with REMPI rather than MPI accomplished in this work. This technique can be used for the spatially-resolved measurements of densities of selective species by single laser pulse. The method has potential to be extended for measurements of 1D or 2D distributions of number densities of selective species.

PUBLICATIONS

1. Journal Publications

1.1 **Sharma, A**., Slipchenko, M. N., Shneider, M. N., Wang, X., Rahman, K. A., & Shashurin, A. Counting the electrons in a multiphoton ionization by elastic scattering of microwave. *Sci. Reports* **8**, 2874 (2018).

1.2 Dhiman, A., **Sharma, A**., Shashurin, A., and Tomar, V. Strontium Titanate Composites for Microwave-Based Stress Sensing. *JOM* **70**, 1811 (2018).

1.3 **Sharma, A.**, Slipchenko, M. N., Rahman, K. A., Shneider, M. N., Shashurin, A. Direct Measurement of Electron Numbers Created at Near-Infrared Laser-Induced Ionization of Various Gases. *J. Appl. Phys.* **125**, 193301 (2019).

1.4 **Sharma, A**., Braun,E. L., Patel, Slipchenko, M. N., Rahman, K. A. Shneider, M. N. & Shashurin, A. "REMPI/MS technique for diagnostics of CO concentration in gaseous mixtures at elevated pressures" (Manuscript in preparation)

2. Conference Proceedings

2.1 **Sharma, A.,** Shashurin, A., Slipchenko, M. Rahman, K. A., Shneider, M. N. Electron density measurement of femtosecond laser induced microplasma filament by microwave scattering *44th IEEE International Conference on Plasma Science (ICOPS)*, May 21 - 25, 2017, Atlantic City, NJ.

2.2 **Sharma, A**., Slipchenko, M. N., Shneider, M. N., Rahman, K. A. & Shashurin, A. Measurements of Electron Numbers in Femtosecond Laser Induced Plasmas Using Rayleigh Microwave Scattering. *AIAA SciTech Forum 2018,* January 8-11, 2018, Orlando, FL.

2.3 **Sharma, A**., Slipchenko, M. N., Shneider, M. N Rahman, K. A. & Shashurin, A. Direct Measurement of Electron Numbers in Multiphoton Ionization of Various Gases. *AIAA Aviation Forum 2018,* June 25-29, 2018, Atlanta, GA.

2.4 **Sharma, A**., Slipchenko, M. N., Shneider, M. N., Rahman, K. A. & Shashurin, A. Absolutely Calibrated REMPI for Diagnostics of Small Neutral Gaseous Components in Mixtures *AIAA SciTech Forum 2019*, January 7-11, 2019, San Diego, CA.

2.5 **Sharma, A.**, Patel, A. R, Slipchenko, M. N., Rahman, K. A., Shneider, M. N., & Shashurin, A. Microwave Detection of REMPI for Diagnostics of Densities of Gaseous Species in Mixtures at Elevated Pressures *AIAA SciTech Forum 2020*, January 6-10, 2020, Orlando, FL.

REFERENCES

1. Siegman, A. E. *Lasers*. (University Science Books, 1986).

2. Torrisi, L. Non-equilibrium plasma produced by intense pulse lasers and relative diagnostics. *Plasma Phys. Control. Fusion* **55**, (2013).

3. Chin, S. L. Femtosecond Laser Filamentation, Ch. 2, 11–48 (Springer-Verlag 2010).
4. Semak, V. V & Shneider, M. N. Electromagnetic beam propagation in nonlinear media. *High Power Laser Sci. Eng.* **3**, (2015).

5. Ledingham, K. W. D. & Singhal, R. P. High intensity laser mass spectrometry — a review. *Int. J. Mass Spectrom. Ion Process.* **163**, (1997).

6. Couairon, A. & Mysyrowicz, A. Femtosecond filamentation in transparent media. *Phys. Rep.* **441**, (2007).

7. Shneider, M. N., Zhang, Z. & Miles, R. B. Simultaneous resonant enhanced multiphoton ionization and electron avalanche ionization in gas mixtures. *J. Appl. Phys.* **104**, 23302 (2008).

8. Tajima, T. & Dawson, J. M. Laser Electron Accelerator. *Phys. Rev. Lett.* **43**, (1979).

9. Malka, V. Principles and applications of compact laser–plasma accelerators. *Nat. Phys.* **4**, (2008).

10. Macklin, J. J., Kmetec, J. D. & Gordon, C. L. High-order harmonic generation using intense femtosecond pulses. *Phys. Rev. Lett.* **70**, (1993).

11. L'Huillier, A. & Balcou, P. High-order harmonic generation in rare gases with a 1-ps 1053-nm laser. *Phys. Rev. Lett.* **70**, (1993).

12. Berge, L., Skupin, S., Nuter, R., Kasparian, J. & Wolf, J. P. Ultrashort filaments of light in weakly ionized, optically transparent media. *Rep. Prog. Phys.* **70**, (2007).

13. Michael, J. B., Edwards, M. R., Dogariu, A. & Miles, R. B. Femtosecond laser electronic excitation tagging for quantitative velocity imaging in air. *Appl. Opt.* **50**, (2011).

14. Keldysh, L. V & others. Ionization in the field of a strong electromagnetic wave. *Sov. Phys. JETP* **20**, 1307–1314 (1965).

15. Voronov, G. S., Delone, G. A., Delone, N. B. & Kudrevatova, O. V. Multiphoton ionization of the hydrogen molecule in the strong electric field of ruby laser emission. *JETP Lett.* **2**, (1965).

16. Popov, V. S. Tunnel and multiphoton ionization of atoms and ions in a strong laser field (Keldysh Theory). *Phys. -Usp.* **47**, (2004).

17. Rahman, K. Patel, M. Slipchenko, T. Meyer, Z. Zhang, Y. Wu, J. Gord, and S. R. Femtosecond, two-photon, laser-induced fluorescence (TP-LIF) measurement of CO in high-pressure flames. *Appl. Opt.* **57**, 5666 (2018).

18. Rahman, K. A. *et al.* Quantitative femtosecond, two-photon laser-induced fluorescence of atomic oxygen in high-pressure flames. *Appl. Opt.* **58**, 1984–1990 (2019).

19. Bodrov, S. Plasma filament investigation by transverse optical interferometry and terahertz scattering. *Opt. Express* **19**, (2011).

20. Ovsyannikov, A. A. & Zhukov, M. F. Plasma Diagnostics, Ch. 4, 59–126 (Cambridge International Science Publishing 2000).

21. Chin, S. L. *Femtosecond Laser Filamentation*. (2010).

22. Talebpour, A., Yang, J. & Chin, S. L. Semi-empirical model for the rate of tunnel ionization of N2 and O2 molecule in an intense Ti:sapphire laser pulse. *Opt. Comm.* **163**, (1999).

23. Talebpourt, A., Larochelle, S. & Chin, S. L. Dissociative ionization of NO in an intense laser field: a route towards enhanced ionization. *J. Phys. B At. Mol. Opt. Phys.* **30**, (1997).

24. Bodrov, S. *et al.* Plasma filament investigation by transverse optical interferometry and terahertz scattering. *Opt. Express* **19**, 6829 (2011).

25. Aleksandrov, N. L. *et al.* Decay of femtosecond laser-induced plasma filaments in air, nitrogen, and argon for atmospheric and subatmospheric pressures. *Phys. Rev. E* **94**, 013204 (2016).

26. Mongin, D. *et al.* Conductivity and discharge guiding properties of mid-IR laser filaments. *Appl. Phys. B* **122**, 267 (2016).

27. Fischer, R. P. *et al.* Conductivity measurements of femtosecond laser-plasma filaments. *IEEE Trans. Plasma Sci.* **35**, 1430 (2007).

28. Mishima, K., Nagaya, K., Hayashi, M. & Lin, S. H. Effect of quantum interference on tunneling photoionization rates of N2 and O2 molecules. *J. Chem. Phys.* **122**, (2005).

29. Zhao, H. *Laser Diagnostics and Optical Measurement Techniques in Internal Combustion Engines*. *Laser Diagnostics and Optical Measurement Techniques in Internal Combustion Engines* (2012). doi:10.4271/r-406.

30. Barlow, R. S. Laser diagnostics and their interplay with computations to understand turbulent combustion. *Proc. Combust. Inst.* **31**, 49–75 (2007).

31. Kohse-Höinghaus, K., Barlow, R. S., Aldén, M. & Wolfrum, J. Combustion at the focus: laser diagnostics and control. *Proc. Combust. Inst.* **30**, 89–123 (2005).

32. Eckbreth, A. C. *Laser diagnostics for combustion temperature and species*. vol. 3 (CRC press, 1996).

33. HS, G., KA, T. & GJ, S. On the effect of carbon monoxide addition on soot formation in a laminar ethylene/air coflow diffusion flame. *Combust. Flame* **156**, 1135–1142 (2009).

34. Lashof, D. A. & Ahuja, D. R. Relative contributions of greenhouse gas emissions to global warming. *Nature* **344**, 529–531 (1990).

35. National Research Council (US) Committee on Acute Exposure Guideline Levels. Acute Exposure Guideline Levels for Selected Airborne Chemicals: Volume 8. Washington (DC): National Academies Press ,US (2010).

36. Wang, J. *et al.* In situ combustion measurements of CO with diode-laser absorption near 2.3 μm. *Appl. Opt.* **39**, 5579–5589 (2000).

37. Schoenung, M. & Hanson, R. K. CO and Temperature Measurements in a Flat Flame by Laser Ab orption Spectroscopy and Probe Techniques. *Combust. Sci. Technol.* **24**, 227–237 (1980).

38. Skaggs, R. R. & Miller, J. H. A study of carbon monoxide in a series of laminar ethylene / air diffusion flames using tunable diode laser absorption spectroscopy. *Combust. Flame* **100**, 430–439 (1995).

39. Awtry, A. R., Fisher, B. T., Moffatt, R. A., Ebert, V. & Fleming, J. W. Simultaneous diode laser based in situ quantification of oxygen, carbon monoxide, water vapor, and liquid water in a dense water mist environment. *Proc. Combust. Inst.* **31**, 799–806 (2007).

40. Boyd, R. W. *Nonlinear Optics, Third Edition*. (Academic Press, Inc., 2008).

41. Attal, B., Pealat, M. & Taran, J.-P. CARS diagnostics of combustion. *J. Energy* **4**, 135–141 (1980).

42. Vestin, F., Afzelius, M. & Bengtsson, P.-E. Development of rotational CARS for combustion diagnostics using a polarization approach. *Proc. Combust. Inst.* **31**, 833–840 (2007).

43. Attal-Trétout, B., Bouchardy, P., Magre, P., Péalat, M. & Taran, J. P. CARS in combustion: Prospects and problems. *Appl. Phys. B* **51**, 17–24 (1990).

44. Haumann, J., Seitzman, J. & Hanson, R. Two-photon digital imaging of CO in combustion flows using planar laser-induced fluorescence. *Opt. Lett.* **11**, 776–778 (1986).

45. Ruchkina, M., Ding, P., Aldén, M., Bood, J. & Brackmann, C. Two-photon-excited fluorescence of CO : Experiments and modeling. *Opt. Express* **27**, 25656–25669 (2019).

46. Aldén, M., Wallin, S. & Wendt, W. Applications of two-photon absorption for detection of CO in combustion gases. *Appl. Phys. B* **33**, 205–208 (1984).

47. Wang, Y. & Kulatilaka, W. D. Spectroscopic investigation of high-pressure femtosecond two-photon laser-induced fluorescence of carbon monoxide up to 20 bar. *Appl. Opt.* **58**, C23--C29 (2019).

48. Rahman, K. A., Athmanathan, V., Slipchenko, M. N., Meyer, T. R. & Roy, S. Pressure-scaling characteristics of femtosecond two-photon laser-induced fluorescence of carbon monoxide. *Appl. Opt.* **58**, 7458–7465 (2019).

49. Brackmann, C. *et al.* Picosecond excitation for reduction of photolytic effects in two-photon laser-induced fluorescence of CO. *Proc. Combust. Inst.* **34**, 3541–3548 (2013).

50. Lee, M. P., Paul, P. H. & Hanson, R. K. Laser-fluorescence imaging of O2 in combustion flows using an ArF laser. *Opt. Lett.* **11**, 7–9 (1986).

51. Lucht, R. P., Salmon, J. T., King, G. B., Sweeney, D. W. & Laurendeau, N. M. Two-photon-excited fluorescence measurement of hydrogen atoms in flames. *Opt. Lett.* **8**, 365–367 (1983).

52. Nefedov, A. P., Sinel'shchikov, V. A., Usachev, A. D. & Zobnin, A. V. Photochemical effect in two-photon laser-induced fluorescence detection of carbon monoxide in hydrocarbon flames. *Appl. Opt.* **37**, 7729–7736 (1998).

53. Rosa, M. D. D. & Farrow, R. L. Temperature-dependent collisional broadening and shift of Q-branch transitions in the B←X(0,0) band of CO perturbed by N2, CO2 and CO. *J. Quant. Spectrosc. Radiat. Transf.* **68**, 363–375 (2001).

54. Shneider, M. N. & Miles, R. B. Microwave diagnostics of small plasma objects. *J. Appl. Phys.* **98**, (2005).

55. Zhang, Z., Shneider, M. N. & Miles, R. B. Microwave diagnostics of laser-induced avalanche ionization in air. *J. Appl. Phys.* **100**, 74912 (2006).

56. Dogariu, A., Shneider, M. N. & Miles, R. B. Versatile radar measurement of the electron loss rate in air. *Appl. Phys. Lett.* **103**, 224102 (2013).

57. Shashurin, A., Shneider, M. N., Dogariu, A., Miles, R. B. & Keidar, M. Temporal behavior of cold atmospheric plasma jet. *Appl. Phys. Lett.* **94**, 231504 (2009).

58. Sawyer, J., Zhang, Z. & Shneider, M. N. Microwave scattering from laser spark in air. *J. Appl. Phys.* **112**, 63101 (2012).

59. Shashurin, A. & Keidar, M. Experimental approaches for studying non-equilibrium atmospheric plasma jets. *Phys. Plasmas* **22**, 122002 (2015).

60. Shashurin, A., Shneider, M. N. & Keidar, M. Measurements of streamer head potential and conductivity of streamer column in cold nonequilibrium atmospheric plasmas. *Plasma Sources Sci. Technol.* **21**, 34006 (2012).

61. Shashurin, A., Shneider, M. N., Dogariu, A., Miles, R. B. & Keidar, M. Temporary-resolved measurement of electron density in small atmospheric plasmas. *Appl. Phys. Lett.* **96**, 171502 (2010).

62. Shashurin, A. Electric discharge during electrosurgery. *Sci. Rep.* **4**, (2014).

63. Wang, X., Stockett, P., Jagannath, R., Bane, S. & Shashurin, A. Time-resolved measurements of electron density in nanosecond pulsed plasmas using microwave scattering. *Plasma Sources Sci. Technol.* **27**, 07LT02 (2018).

64. Wang, X. & Shashurin, A. Study of atmospheric pressure plasma jet parameters generated by DC voltage driven cold plasma source. *J. Appl. Phys.* **122**, 63301 (2017).

65. Raizer, Y. P. *Gas Discharge Physics*. (1991).

66. Jones, R. C. A generalization of the dielectric ellipsoid problem. *Phys. Rev.* **68**, (1945).

67. Leonov, S. B. Femtosecond laser guiding of a high-voltage discharge and the restoration of dielectric strength in air and nitrogen. *Phys. Plasma.* **19**, (2012).

68. Jackson, J. D. Classical Electrodynamics, 3rd Edition (Wiley Hoboken 1998).

69. Pozar, D. M. Microwave Engineering, Ch. 14, 658–711 (Wiley Hoboken 2012).

70. Shneider, M. N., Zheltikov, A. M. & Miles, R. B. Tailoring the air plasma with a double laser pulse. *Phys. Plasmas* **18**, (2011).

71. Koechner, W. Solid –State Laser Engineering, 5th Edition (Springer, 2006).

72. Semak, V. V & Shneider, M. N. Effect of power losses on self-focusing of high-intensity laser beam in gases. *J. Phys. D. Appl. Phys.* **46**, 185502 (2013).

73. Tjossem, P. J. H. & Smyth, K. C. Multiphoton excitation spectroscopy of the B 1Σ+ and C 1Σ+ Rydberg states of CO. *J. Chem. Phys.* **91**, 2041–2048 (1989).

74. Fiechtner, G. J. & Gord, J. R. Absorption and the dimensionless overlap integral for two-photon excitation. *J. Quant. Spectrosc. Radiat. Transf.* **68**, 543–557 (2001).

75. Li, B. *et al.* Comprehensive CO detection in flames using femtosecond two-photon laser-induced fluorescence. *Opt. Express* **25**, 25809 (2017).

76. Settersten, T. B., Dreizler, A. & Farrow, R. L. Temperature- and species-dependent quenching of CO B probed by two-photon laser-induced fluorescence using a picosecond laser. *J. Chem. Phys.* **117**, 3173–3179 (2002).

77. Qin, Z., Zhao, J. M. & Liu, L. H. Radiative transition probabilities for the main diatomic electronic systems of N2, N2+, NO, O2, CO, CO+, CN, C2 and H2 produced in plasma of atmospheric entry. *J. Quant. Spectrosc. Radiat. Transf.* **202**, 286–301 (2017).

78. Rosa, M. D. Di & Farrow, R. L. Cross sections of photoionization and ac Stark shift measured from Doppler-free B ← X(0,0) excitation spectra of CO. *J. Opt. Soc. Am. B* **16**, 861–870 (1999).

APPENDIX A

Calculating the intensity integral

We present calculation of laser intensity integral over spatial and temporal variables:

$$\int\int I(r,z,t)^8 dtdV = \frac{231\pi}{1024\cdot 16}\sqrt{\frac{\pi}{8}}{I_0}^8 \pi w_0^2 z_R \tau$$

The integration is first taken over time period when laser pulse exists at particular location of space and then spatial integral is taken over region where laser beam presents. For the specific system utilized in current experiment, main contribution to the temporal integral is gained during the laser pulse time of τ=98.6 fs, while spatial integral is accumulated primarily in vicinity of the beam waist where intensity is maximal.

The limits of the integrals can be extended to infinity when analytical approximation space-time dependence of the laser pulse in the form of

$$I(r,z,t) = I_0 \frac{w_0^2}{w(z)^2} e^{-\frac{2r^2}{w(z)^2}} e^{-\frac{(t-t^*(r,z))^2}{\tau^2}}$$

with

$$w(z) = w_0\sqrt{1+\left(\frac{z}{z_R}\right)^2}$$

is used:

$$\int\int I(r,z,t)^8 dtdV = \int_{-\infty}^{+\infty}\int_{0}^{+\infty}\int_{-\infty}^{+\infty} {I_0}^8 \frac{w_0^{16}}{w(z)^{16}} e^{-\frac{16r^2}{w(z)^2}} e^{-\frac{8(t-t^*(r,z))^2}{\tau^2}} 2\pi r\, dt\, dr\, dz$$

Inner temporal integral can be calculated analytically by changing of variables to

$$\tilde{t} = \frac{\sqrt{8}(t-t^*(r,z))}{\tau}$$

for any finite (r,z)-location

$$\int_{-\infty}^{+\infty} e^{-\frac{8(t-t^*(r,z))}{\tau^2}} dt = \frac{\tau}{\sqrt{8}} \int_{-\infty}^{+\infty} e^{-\tilde{t}^2} d\tilde{t} = \sqrt{\frac{\pi}{8}}\tau.$$

The outer spatial integral can be first simply calculated over r – variable and then using standard integral $\int_{-\infty}^{+\infty} \frac{1}{[1+x^2]^7} dx = \frac{231\pi}{1024}$.

This finally yields:

$$\int\int I(r,z,t)^8 dt dV$$

$$= {I_0}^8 \sqrt{\frac{\pi}{8}}\tau \int_{-\infty}^{+\infty}\int_{0}^{+\infty} \frac{w_0^{16}}{w(z)^{16}} e^{-\frac{16r^2}{w(z)^2}} 2\pi r dr dz = {I_0}^8 \sqrt{\frac{\pi}{8}}\tau \int_{0}^{+\infty} \frac{\pi w_0^{16}}{16} \frac{1}{w(z)^{14}} dz$$

$$= {I_0}^8 \sqrt{\frac{\pi}{8}}\tau \frac{\pi w_0^2}{16} \int_{-\infty}^{+\infty} \frac{1}{\left[1+\left(\frac{z}{z_R}\right)^2\right]^7} dz$$

$$= {I_0}^8 \sqrt{\frac{\pi}{8}}\tau \frac{\pi w_0^2}{16} \frac{231\pi}{1024} z_R$$